

AperTO - Archivio Istituzionale Open Access dell'Università di Torino

Deformation and temperature variation along thrust-sense shear zones in the hinterland-foreland transition zone of collisional settings: A case study from the Barbagia Thrust (Sardinia, Italy)

This is the author's manuscript

Original Citation:

Availability:

This version is available <http://hdl.handle.net/2318/2051871> since 2025-02-14T09:44:01Z

Published version:

DOI:10.1016/j.jsg.2022.104640

Terms of use:

Open Access

Anyone can freely access the full text of works made available as "Open Access". Works made available under a Creative Commons license can be used according to the terms and conditions of said license. Use of all other works requires consent of the right holder (author or publisher) if not exempted from copyright protection by the applicable law.

(Article begins on next page)

Journal Pre-proof

Deformation and temperature variation along thrust-sense shear zones in the hinterland-foreland transition zone of collisional settings: A case study from the Barbagia Thrust (Sardinia, Italy)

A. Petroccia, R. Carosi, C. Montomoli, S. Iaccarino, A. Vitale Brovarone

PII: S0191-8141(22)00132-8

DOI: <https://doi.org/10.1016/j.jsg.2022.104640>

Reference: SG 104640

To appear in: *Journal of Structural Geology*

Received Date: 10 February 2022

Revised Date: 30 May 2022

Accepted Date: 3 June 2022

Please cite this article as: Petroccia, A., Carosi, R., Montomoli, C., Iaccarino, S., Vitale Brovarone, A., Deformation and temperature variation along thrust-sense shear zones in the hinterland-foreland transition zone of collisional settings: A case study from the Barbagia Thrust (Sardinia, Italy), *Journal of Structural Geology* (2022), doi: <https://doi.org/10.1016/j.jsg.2022.104640>.

This is a PDF file of an article that has undergone enhancements after acceptance, such as the addition of a cover page and metadata, and formatting for readability, but it is not yet the definitive version of record. This version will undergo additional copyediting, typesetting and review before it is published in its final form, but we are providing this version to give early visibility of the article. Please note that, during the production process, errors may be discovered which could affect the content, and all legal disclaimers that apply to the journal pertain.

© 2022 Published by Elsevier Ltd.



Credit author contribution statement

Petroccia A.: Conceptualization, Investigation, Writing – original draft, Data curation, Visualization, Validation, Formal analysis;

Carosi R.: Conceptualization, Investigation, Writing – review and editing, Supervision, Securing of funds, Project administration;

Montomoli C.: Conceptualization, Investigation, Writing – review and editing, Supervision, Securing of funds, Project administration;

Iaccarino S.: Conceptualization, Investigation, Writing – review and editing, Supervision, Securing of funds, Project administration;

Vitale Brovarone A.: Review and editing, Supervision.

15 Abstract

16 In the Internal Zone of a continental collisional orogen, first-order contractional shear zones accommodate crustal
17 shortening. Structural investigations at different scales, flow kinematics, and finite strain analyses are fundamental
18 tools to determine how deformation is accommodated and partitioned. Spatial temperature variations can be
19 responsible for the dynamic weakening and strain localization in the crust, therefore understanding the thermal
20 conditions of shearing and deformation is critical. We integrate field observations, meso- and microstructural
21 analyses, kinematic vorticity estimations, and finite strain data with a quantitative thermometric analysis by Raman
22 spectroscopy on carbonaceous material along a ductile shear zone: the Barbagia Thrust (BT) in the hinterland-
23 foreland transition zone of the Sardinian Variscan belt. These analyses, performed in two different parts of the
24 shear zone, yield similar finite strain gradients, albeit with an increasing component of simple shear with increasing
25 temperature, highlighting the feedback between temperature and vorticity. Our results are best by a tectonic
26 scenario with shear heating, where higher magnitude gradients correspond to higher vorticity and finite strain
27 values, which indicate greater shear and heating values. The heating quantified along the BT is compared favorably
28 to numerical and mechanical models (~50 °C). We demonstrate how the BT represents a major tectonic boundary
29 separating the internal sector belonging to the metamorphic core of the belt from the external one involved in the
30 orogenic wedge system.

31 Keywords:

32 Shear zone; kinematic vorticity; RSCM; Variscan belt; Nappe Zone

33 1. Introduction

34 The geodynamic evolution of collisional orogens has been classically described using an orogenic wedge model,
35 where different rock packages experience different finite metamorphic histories (e.g., Platt, 1993; Jaquet et al.,
36 2018; Malavieille et al., 2019). The hinterland-foreland transition zone making the fold-and-thrust belt is defined
37 by the progressive transition from tectonic units occurring in the metamorphic core of the belt to the ones deformed
38 at shallower crustal levels and steadily included in the orogenic wedge (Larson et al., 2010; Thigpen et al., 2010,

39 2017; Schneider et al., 2014; Montomoli et al., 2018). The first theoretical models applied to the hinterland-
40 foreland transition zone were initially developed within a critical-wedge framework wherein thrust behavior is
41 dominantly brittle and occurs along discrete planes (e.g., Elliott, 1976; Dahlen et al., 1984). Recent, it is well-
42 noted that during orogenic belt formation, large sectors of crustal rocks exhibit ductile and brittle-ductile
43 deformation (e.g., Platt, 1986; Grasemann et al., 1999; Steck, 2008; Steck et al., 2013; Jaquet et al., 2018).

44 Hinterland-foreland transition zones are characterized by the presence of mylonitic rocks along km-scale ductile
45 shear zones linked to thrust-sense shear zones, which lead to the formation of thrust sheets or tectonic nappes.
46 Classically, these zones have been associated with a simple shear-dominated deformation (e.g., Coward and Kim,
47 1981; Mitra, 1994; Seno et al., 1998; Yonkee, 2005). However, quantitative studies have shown that the ductile
48 deformation in the thrust-sense shear zone involves a significant component of pure shear deformation (e.g.,
49 Simpson and De Paor, 1993; Grasemann et al., 1999; Ring and Brandon, 1999; Bailey et al., 2007; Ring and
50 Kumerics, 2008; Law et al., 2021). Therefore, shear zones in dynamics orogenic wedge settings require a
51 quantitative assessment of the kinematic vorticity (Xypolias, 2010; Thigpen et al., 2010, 2013; Fossen and
52 Cavalcante, 2017; Ghosh et al., 2020, Simonetti et al., 2020a, b).

53 Several processes can potentially be responsible for the dynamic weakening and strain localization in the crust,
54 including (i) shear heating (e.g., Brun and Cobbold, 1980; Molnar and England, 1990; Camacho et al., 2001; Burg
55 and Schmalholz, 2008; Thielmann and Kaus, 2012; Platt, 2015, 2018; Regenauer-Lieb et al., 2015), (ii) fabric
56 development (e.g., Montési, 2013), and (iii) grain-size reduction by cataclasis or dynamic recrystallization (e.g.,
57 Montési and Zuber, 2002; Handy et al., 2007; Platt and Behr, 2011). Among them, thermal weakening (Takeuchi
58 and Fialko, 2012; Willis et al., 2019), linked to shear heating, has been regarded as one of the main mechanisms
59 in localizing deformation and for the development of shear zones (e.g., Schott et al., 2000; Thielmann and Kaus,
60 2012; Duretz et al., 2014). This mechanism is particularly applicable to the middle crust close to the brittle/ductile
61 transition (e.g., Hirth et al., 2001; Behr and Platt, 2014; Platt, 2015). Thus, establishing the thermo-kinematic
62 setting of shear zones is crucial because it is one of the most effective ways to test theoretical models of orogen-

63 tectonometamorphic evolution against field observations (e.g., Sanderson, 1982; Ring et al., 2001; Law et al.,
64 2004; Thigpen et al., 2021; Iaccarino et al., 2020; Waters et al., 2018).

65 Several works have used a multidisciplinary approach to unravel the deformational, structural, and thermal
66 gradients of a region and, in turn, discriminate marginal and central areas within high strain shear zones (Xypolias,
67 2010; Ring et al., 2015; Carosi et al., 2020; Grujic et al., 2020; Simonetti et al., 2020a, b, 2021). Field-based
68 studies, combined with vorticity and kinematic analysis, are key for exploring shear zone evolution. There are
69 several analytical techniques to determine both the kinematic vorticity and the deformation temperature in
70 mylonitic rocks. Whereas kinematic vorticity estimation can be generally obtained from all kinds of deformed
71 rocks, low-grade metasedimentary sequences in the hinterland-foreland transition zone contain mineralogical
72 assemblages that are not always suitable for conventional thermometric techniques.

73 The Raman spectroscopy on carbonaceous material (RSCM; Beyssac et al., 2002, 2003, 2004) is based on the
74 progressive transformation of carbonaceous material (CM) to graphite with increasing temperature. RSCM has
75 generally been used as a geothermometer to determine the peak temperature reached during burial or tectonic
76 thrust stacking (Chen et al., 2011; Scharf et al., 2013; Vitale Brovarone et al., 2013; Bellanger et al., 2015; Molli
77 et al., 2018; Berger et al., 2020; Pérez-Cáceres et al., 2020; Montmartin et al., 2021; Nibourel et al., 2021), during
78 contact metamorphism (Aoya et al., 2010; Mori et al., 2017; Beyssac et al., 2019; Skrzypek, 2021) or during
79 frictional heating along fault planes after an earthquake (Fauconnier et al., 2014; Kaneki et al., 2016; Kuo et al.,
80 2017, 2018; Nakamura et al., 2020; Muirhead et al., 2021). It is non-destructive and sensitive to thermal changes,
81 enabling to constrain peak temperature in rocks from different geological contexts and metamorphic conditions
82 (see Henry et al., 2019 for a complete review).

83 The hinterland-foreland transition zone of the Sardinian Variscan belt in Italy is a well-preserved low- to medium-
84 grade Variscan basement that was not overprinted by subsequent Alpine orogenesis. It represents an excellent site
85 to investigate a regional thrust-sense movement shear zone related to the nappe emplacement during the
86 continental collision in the Early Carboniferous, i.e., the Barbagia Thrust (BT; Carosi and Pertusati, 1990; Carosi
87 and Malfatti, 1995; Montomoli et al., 2018). The BT marks the boundary between the Internal and the External

88 Nappe Zone of the Variscan belt, separating tectonic units with a complex pressure-temperature-time (P-T-t)
89 history from tectonic units deformed at a higher structural level during the progressive propagation of deformation
90 from the hinterland to the foreland (Montomoli et al., 2018). It played a critical role during nappe stacking and the
91 exhumation of the crustal units. Few studies have addressed the structure, kinematics, and flow regime of the BT
92 (e.g., Montomoli et al., 2018), and its thermal architecture is poorly understood.

93 To better constrain the structural architecture and the thermal evolution of the BT, we collected data in two
94 thermally- and potentially kinematically-distinct sectors of the shear zone. In this study, we defined the thermo-
95 structural evolution of the BT within the Nappe Zone by combining detailed field observations, meso- and
96 microstructural analysis, vorticity analysis, and finite strain estimations with a quantitative thermometric analysis
97 by RSCM. Variations in both temperature conditions of shearing and magnitude of simple shear between these
98 two domains allow us to examine any linkages and feedbacks between shear heating and thrust kinematics.

99 2. Overview of the Sardinian Variscan belt

100 The continent-continent collision between Laurentia–Baltica and Gondwana is responsible for the deformation of
101 the Sardinian Paleozoic basement (Carmignani et al., 1994) during the Variscan orogeny (Matte, 2001). The
102 Sardinian metamorphic belt (Carmignani et al., 2001, 2015; see Cruciani et al., 2015 for a review) is made up of:
103 (i) the External Zone, (ii) the Axial Zone or the hinterland of the belt and (iii) the Nappe Zone or hinterland-
104 foreland transition zone (Fig. 1a).

105 (insert Figure 1 here)

106 The Nappe Zone of central and southern Sardinia has received considerable attention over the last 40 years
107 (Carmignani and Pertusati, 1977; Carmignani et al., 1982, 1994, 2015; Carosi et al., 1991; Conti et al., 1998, 1999,
108 2001; Franceschelli et al., 2005; Casini et al., 2010; Cocco and Funedda, 2011, 2017; Cocco et al., 2018). It has
109 been subdivided into External (central to southern Sardinia) and Internal (northern to central Sardinia) Nappe Zone
110 (Fig. 1a). The lithostratigraphic succession is similar in both nappes. The main difference is the relative paucity of

111 Ordovician metavolcanic rocks in the Internal Nappe Zone sequence (Carmignani et al., 1994) compared to the
112 External Nappe Zone.

113 The Internal Nappe Zone (Fig. 1a) comprises: (i) the Low-Grade Metamorphic Complex (LGMC; Barbagia,
114 Goceano, and southern Nurra units; Vai and Cocozza, 1974; Carmignani et al., 1994; Pertusati et al., 2002;
115 Montomoli, 2003) which reached greenschist-facies metamorphic conditions, and (ii) the Medium-Grade
116 Metamorphic Complex (MGMC; Baronie, Anglona, and northern Nurra units; Carmignani et al., 1994, 2001)
117 which reached amphibolite-facies conditions (Cruciani et al., 2015; Carosi et al., 2020). The boundary zone
118 between the Internal Nappe Zone and the High-Grade Metamorphic Complex is marked by the Posada-Asinara
119 shear zone (PASZ; Carosi et al., 2020 and references therein; Fig. 1a), a dextral transpressive Late-Variscan shear
120 zone (Carosi et al., 2002), active from ~325 up to ~300 Ma (Di Vincenzo et al., 2004; Carosi et al., 2012; 2020).

121 In the External Nappe Zone, five main tectonic units have been identified, which include according to the lowest
122 to the hishest unit in the pile (Fig. 1b): (1) Monte Grighini Unit, (2) Riu Gruppa/Castello Medusa Unit, (3) Gerrei
123 Unit, (4) Meana Sardo Unit and, finally, (5) Sarrabus Unit (Calvino, 1959; Carosi et al., 1991; Musumeci, 1992;
124 Carmignani et al., 1994; Conti et al., 2001; Barca et al., 2003; Funedda et al., 2011, 2015; Pavanetto et al., 2012;
125 Cocco et al., 2018). All these units are characterized by syn-tectonic regional greenschist-facies metamorphism
126 (Carmignani et al., 1994; Carosi et al., 1991, 2010; Franceschelli et al., 1992), except for the Monte Grighini Unit.
127 Illite and chlorite crystallinity values report anchizonal-epizonal metamorphic conditions for the External Nappe
128 Zone (Franceschelli et al., 1992; Carosi et al., 2010; Montomoli et al., 2018). The boundary between the Internal
129 and the External nappes is defined by a regional-scale thrust-sense shear zone that developed a pervasive high-
130 strain mylonitic zone, i.e., the BT (Carosi and Malfatti, 1995; Montomoli et al., 2018).

131 Several authors have documented a complex structural evolution of both Internal and External Nappe Zone
132 (Carmignani and Pertusati, 1977; Carmignani et al., 1982, 1994; Dessau et al., 1982; Carosi and Pertusati, 1990;
133 Carosi et al., 1991, 2002, 2004; Conti and Patta, 1998; Conti et al., 1998; Funedda, 2009; Montomoli et al., 2018).
134 D₁ and D₂ deformation phases are related to continental collision and thrust related shortening, responsible for
135 nappe emplacement. These are followed by later D₃ and D₄ tectonic phases (Conti et al., 1998, 2001; Carosi et al.,

136 2002, 2004) that represent the end of the collisional shortening (D_3 phase) and the collapse of the belt (D_4 phase).
137 The latter is regarded as nearly contemporaneous with the emplacement of the Sardo-Corso batholith at ~320-280
138 Ma (Del Moro et al., 1975; Casini et al., 2012).

139 We focused on two key sectors, Area I and II, for the northern and the southern investigated selected areas,
140 respectively (Fig. 1b), of the hinterland-foreland transition zone (Fig. 1b). Here, the contact between the Internal
141 and External Nappe Zone (i.e., the Barbagia Thrust) is marked by a well-exposed mylonitic zone. Both areas are
142 located in the Barbagia region (Central Sardinia), along with the northern and the southern limb of the Barbagia
143 Synform (Fig. 1b, c). Area I and II are ~20 km apart. The Internal Nappe Zone is represented by the structurally
144 upper Barbagia Unit (BU), in the hangingwall (HW), overthrust on the Meana Sardo Unit (MSU), in the footwall
145 (FW), belonging to the External Nappe Zone (Fig. 1b, c). The structural maps, the cross-sections, the projection
146 of structural data, and the position of the analyzed samples are reported in Figure 2a,b and in Figure 3a,b.
147 (insert Figure 2 here)

148 3. Meso- and microstructural analysis results

149 In both Area I and II, four main phases of ductile deformation were observed based on overprinting criteria and
150 structural observations from the meso- to microscale. Microstructural analyses were performed on field-oriented
151 samples, cut perpendicular to the main foliation and parallel to the object lineation (approximating the XZ section
152 of the finite strain ellipsoid). Folds have been described following Ramsay (1967). Dynamic deformation
153 mechanisms for both quartz and feldspar have been described according to Pryor (1993), Piazzolo and Passchier
154 (2002), Stipp et al. (2002) and Law (2014). Foliations, kinematic indicators, and mylonites have been classified
155 according to Passchier and Trouw (2005). Mylonite has been classified considering the percentage of the matrix
156 as compared to porphyroclasts, varying from 50-90% for mylonitic rocks to more than 90% for ultramylonite.
157 Mineral abbreviations are after Whitney and Evans (2010) except for white mica (Wm).

158 (insert Figure 3 here)

159 3.1. D_1 and D_2 deformation phases

160 Relicts of the original bedding (S_0) can be recognized as a compositional alternation (Fig. 4a) or dismembered
161 lentoid fragments only far from the BT. D_1 phase is well-expressed far from the BT and mainly in FW. Fold
162 systems related to the D_1 phase are only observed in Area II within the External Nappe Zone, far from the BT.
163 They show a S-SW vergence (Fig. 4b) and are moderately to strongly asymmetric. In most cases, the D_1 signature
164 is represented by the S_1 foliation, parallel or at a moderate angle to the bedding (S_0 ; Fig. 4b). Often, due to complete
165 transposition, it is nearly impossible to distinguish S_1 from S_0 ($S_1//S_0$). The S_1 can be recognized within the
166 thickened hinges of F_2 folds and in microlithons (Fig. 4c). At the microscale, S_1 is a continuous foliation defined
167 by syn-kinematic recrystallization of white mica (Fig. 4c), chlorite, quartz, calcite, opaque minerals, and rare albite.
168 Moving toward the BT high-strain zone, a well-developed transposition of S_1 and rootless folds (Fig. 4d) has been
169 recognized.

170 Structures related to the D_2 phase are characterized by tight to isoclinal, overturned to recumbent folds, with a S-
171 SW vergence, developed from micro- to map-scale. The interlimb angles of F_2 folds range from $60-2^\circ$ (close to
172 sub-isoclinal; Fig. 4d), and they generally show rounded and thickened hinges with stretched limbs (class 2 of
173 Ramsay, 1967; Fig. 4d). The F_2 folds show an S_2 foliation parallel or sub-parallel to the relative fold axial planes,
174 and it generally represents the main foliation at the outcrop-scale. S_2 mainly strikes E-W with both local NNW-
175 SSE and NNE-SSW. In Area I, S_2 dips to the S with local variations toward the N (Fig. 2a) due to late deformation,
176 while in Area II (Fig. 3a), S_2 dips toward the N. F_2 fold axes show the main E-W trend gently plunging with quite
177 scattered values in both Area I and II (Fig. 2b, 3b). A well-visible N-S or NE-SW trend (Fig. 2b, 3b) of the object
178 lineation L_2 on the S_2 foliation is recognizable (Fig. 4e). The F_2 fold axes are nearly perpendicular to the L_2 .
179 Moving toward the BT, the main anisotropy gradually changes from a gradational to discretely spaced crenulation
180 cleavage to a continuous S_2 foliation defined mainly by chlorite + white mica (Fig. 4f). The intensity of strain
181 increases toward the tectonic contact, as does the mylonitic foliation. It is worth noting that the frequency of the
182 occurrence of the D_1 structures decreases approaching the BT.

183 (insert Figure 4 here)

184 *3.2. The Barbagia Thrust*

185 In both Area I and II, located along the northern and southern limb of the Barbagia Synform, the BT is
186 characterized by a hm-thick mylonitic zone that shows a similar deformation pattern. The BT-related structures
187 (D_2) overprint both metasedimentary and metavolcanic or metavolcanoclastic rocks of the FW and metasandstone,
188 metasilstone, and metapsammite of the HW (see the geological maps in Figs. 2a and 3a), transposing all previous
189 structures. In the FW and HW of the BT, a variation in structural style moving toward the BT across the
190 deformation gradient is present. The intensity of deformation increases toward the BT, where folds become tighter
191 and lineation more pervasive; contemporaneously, the spacing between foliation domains decreases. Approaching
192 the high strain zone, the mylonitic foliation obliterates the previous S_1 foliation and microlithons. Although Area
193 I and II are located in different sectors of the F_3 Barbagia Synform, they are characterized by the same shear sense.

194 Sheared metasedimentary rocks belonging to the FW (San Vito Fm.) and the HW (Filladi del Gennargentu Fm.)
195 are characterized by a transition from a well-developed discrete smooth spaced foliation with zonal cleavage
196 domains (Fig. 5a) up to a continuous cleavage (Fig. 5b) approaching the BT. In samples from the high-strain zone,
197 a penetrative continuous mylonitic foliation is found. The mylonitic S_2 foliation is defined by elongated quartz
198 grains and phyllosilicate-rich levels, dominated by chlorite + white mica (Fig. 5b). Patchy undulose extinction
199 (Fig. 5c) and small new grains are recognizable in quartz. These structures suggest that bulging mechanisms (BLG
200 II) with minor and local subgrain rotation recrystallization (SGR; Fig. 5d) are the main deformation mechanisms
201 in quartz (Stipp et al., 2002; Law, 2014). Kinematic indicators with a top-to-the S/SW sense are represented by a
202 meso- (Fig. 5e) and microscale (Fig. 5f) C' - S fabric, asymmetric porphyroclasts and rare asymmetric
203 displacement-controlled strain fringes around rigid objects, mainly constituted by pyrite.

204 In the FW, metavolcanic and metavolcanoclastic rocks belonging to the Santa Vittoria Fm., a progressive transition
205 from non-sheared rocks to mylonites (Fig. 5g) to ultramylonites (Fig. 5h) can be observed along the deformation
206 gradient approaching the BT. This is coupled with a gradual variation from a disjunctive cleavage with sub-parallel
207 cleavage domains to a continuous cleavage in the most intensely deformed ultramylonitic rocks. In mylonites, the
208 main foliation is defined by grain shape preferred orientation of feldspar, quartz, white mica, and chlorite (Fig.
209 5g). Feldspars show undulose extinction, evidence of brittle deformation, and locally flame perthite. In

210 ultramylonite, the matrix is composed of ultra-fine-grained black bands made by phase-mixing of white mica
211 surrounding rounded K-feldspar (Fig. 5h) and plagioclase porphyroclasts. The fine grain size ($< 25 \mu\text{m}$) of quartz
212 in these rocks prohibits the identification of their recrystallization mechanisms. Kinematic indicators include C'-
213 S fabrics, mica fish, and the asymmetry of porphyroclasts (Fig. 5h) of quartz or feldspar crystals which indicate a
214 top-to-the S-SW sense of shear.

215 (insert Figure 5 here)

216 3.3. D_3 and D_4 deformation phases

217 The D_3 phase is composed of m- to km-scale folds (i.e., Gennargentu Antiform and Barbagia Synform) that
218 overprint and refold all previous structural elements, including the BT (Fig. 6a). They are commonly gentle,
219 slightly asymmetric, and open, ranging from upright to steeply inclined and from metric to pluri-m long
220 wavelengths (Fig. 6a, b). Locally kink type folds occur (Fig. 6c). These folds display a S-SE vergence (Fig. 6a, b,
221 c) with local variation to N. A_3 axes generally are coaxial to the A_2 axes and perpendicular to the L_2 object lineation
222 in both investigated areas (Figs. 2b and 3b). In the F_3 hinge zones of less competent units, the S_3 axial-plane
223 foliation is represented by a gradational crenulation cleavage (Fig. 6d). The main deformation mechanisms, as
224 seen at the microscale, are pressure solution and kinking in phyllosilicate-rich domains (Fig. 6e). No metamorphic
225 mineral assemblage related to these folds has been observed (Fig. 6e). D_4 produced gentle to open F_4 folds with
226 sub-horizontal axes and axial planes (Fig. 6f). Locally, some minor-scale kink-folds occur. No metamorphic
227 mineral assemblages related to the D_4 phase have been observed.

228 (insert Figure 6 here)

229 4. Kinematic vorticity and finite strain results

230 In order to characterize the type of flow within the BT, kinematic vorticity analyses were performed on mylonitic
231 samples in both Area I and II (Figs. 2a and 3a). In the present study, the C' shear band method (Kurz and Northrup,
232 2008; Gillam et al., 2013) and two different porphyroclast-based methods, the porphyroclast aspect ratio method
233 (PAR; Passchier, 1987; Wallis et al., 1993) and the rigid grain net method (RGN; Jessup et al., 2007), have been

234 applied. See Appendix 1 for a detailed description of the different methods. A total of 19 samples (8 for HW and
235 11 for FW) were selected (Table 1). Examples of polar histograms related to C' shear band method (sample AP19-
236 37), used to derive the angle ν , are provided in Figure 7a. For the RGN and PAR methods, an example of the same
237 sample (sample AP19-37) is shown in Figure 7b, c, respectively. An example (sample AP19-39B) of the Fry
238 diagram for both the XZ and YZ sections of the finite strain ellipsoid is presented in Figure 7d. Full results are
239 provided in Appendix 2, 3, and 4. The complete finite strain dataset (samples locations in Figs. 2a and 3a), obtained
240 by the centre-to-centre method, is reported in Table 1.

241 (insert Figure 7 and Table 1 here)

242 4.1. Area I

243 In Area I, a total of 9 samples (3 for HW and 6 for FW, respectively; Fig. 2a) analyzed with the C' shear band
244 method gives (Table 1) a vorticity number ranging from 0.50 to 0.93, with a mean of 0.71. In sample AP19-37,
245 from the FW, we found, applying the stable porphyroclasts method, a minimum R_c of 1.98 and a maximum R_c of
246 2.20 corresponding to W_k values of 0.59 and 0.66 (Table 1), respectively. In sample LA-14, from the FW,
247 minimum and maximum R_c values are 2.11 and 2.33, corresponding to W_k between 0.63 and 0.69 (Table 1). The
248 overlapping but different range of vorticity (Fig. 8a) in these samples may be due to (i) different analytical
249 uncertainties associated with input data and/or (ii) the different strain memory. Finite strain results in Area I
250 indicate an axial ratio of 2.18, 2.65, and 3.30 on the XZ sections, 1.42, 1.62, and 1.26 on YZ sections of the finite
251 strain ellipsoid and the shape parameter of the strain ellipsoid (K) is 1.27, 1.03 and 6.23 for samples AP19-125,
252 AP19-39B, and 2021_81A, respectively (Fig. 7b). Mylonite in the middle part of the shear zone (samples AP19-
253 39B) is close to plane strain conditions, whereas mylonite closest to the core of the BT (sample 2021_81A) is in
254 the prolate field (Fig. 7c).

255 4.2. Area II

256 Data from Area II, obtained from 9 samples analyzed by the C' shear band method (5 for HW and 4 for FW,
257 respectively; see Fig. 3a for sample location and Table 1 for results), give a vorticity number ranging from 0.50 to

258 0.90, with a mean of 0.67. In Area II, finite strain results indicate an axial ratio of 1.96, 2.25, and 2.42 on the XZ
259 sections and 1.49, 1.63, 1.36 on YZ sections of the finite strain ellipsoid and the shape parameter of the strain
260 ellipsoid (K) is 0.39, 0.61 and 2.17 for samples 2021_56B, 2021_56A, and 2021_40B, respectively. In the Flinn
261 diagram (Fig. 8b), the two farthest samples with respect to the core of the BT (samples 2021_56A and 2021_56B)
262 fall in the oblate field near the plane strain conditions. Finite strain in mylonite in the external part of the shear
263 zone (AP19-125) plots close to plane strain conditions, whereas in samples closest to the core of the BT (sample
264 2021_40B) is in the prolate field (Fig. 7c).

265 Estimated values in both Area I and II reveal an important contribution of pure shear during thrust-sense ductile
266 deformation (Fig. 8a). Moreover, the results highlight in both areas, a strong increase of the component of simple
267 shear along the deformation gradient in both units, approaching the BT high-strain zone (Fig. 8a, Table 1).

268 (insert Figure 8 here)

269 **5. RSCM estimates**

270 The peak temperature was obtained using RSCM. This method is based on the progressive transformation of CM
271 during the increase of temperature, and it is not affected by the retrograde history (Beysac et al., 2002; Beysac
272 and Lazzeri, 2012). The RSCM temperature estimates, discussed in the following sections, were derived from the
273 Aoya et al. (2010) calibration (see Appendix 1 for a detailed description of the RSCM procedure). The temperature
274 results, calculated with both Beysac et al. (2002) and Aoya et al. (2010) calibrations, are given in Table 1. A total
275 of 18 samples, from both Area I and Area II (Figs. 2a and 3a for sample location) collected at different structural
276 positions, were selected for RSCM analysis. Representative spectra and corresponding RSCM temperatures are
277 reported in Fig. 9a, b, respectively.

278 (insert Figure 9 here)

279 **5.1. Area I**

280 In Area I, the R2 parameter ranges from 0.30 to 0.41 with an average of 0.35. The R2 parameter varies from 0.30
281 to 0.40 and from 0.31 to 0.41 for the HW and FW, respectively (Table 1). We detected a systematic increase in
282 temperature moving from the structurally higher parts of the HW, or from the structurally lower parts of the FW,
283 moving into the BT core, from ~455 up to 508 °C (Fig. 9a). In particular, within the HW, temperature increases
284 along the deformation gradient from a minimum of ~454 up to 502 °C close to the BT. The Raman spectra of the
285 FW follow the same pattern and temperature increases from ~444 °C up to ~496 °C for the sample nearest to the
286 BT. The lowest temperatures in Area I have been found in non-mylonitic samples, where relict S₁ foliation is
287 observable in microlithons (Fig. 10a). No systematic differences in the obtained RSCM T results have been
288 detected from graphite lying on S₁ or S₂. Samples with the highest temperature have been found in mylonitic rocks
289 within the core of the BT (Fig. 10b).

290 5.2. Area II

291 In Area II, the R2 parameter ranges from 0.29 to 0.48, with an average of 0.36. The R2 parameter varies from 0.42
292 to 0.29 and from 0.48 to 0.31 for the HW and FW, respectively (Table 1). Moving from the structurally higher
293 sectors of the HW, or from the structurally lower one of the FW, toward the BT, we highlighted a general increase
294 in temperature, from ~420 up to 505 °C (Fig. 9b). Along the deformation gradient, temperature increases from
295 ~420 up to 497 °C and ~443 up to 505 °C for FW and HW, respectively. As for Area I, the lowest temperatures in
296 Area II have been detected in non-mylonitic samples (Fig. 10a) and no differences have been detected from
297 graphite lying on S₁ or S₂. Samples with the highest temperature have been found in mylonites from both HW and
298 FW (Fig. 10b).

299 (insert Figure 10 here)

300 6. Discussion

301 6.1. Geometry and deformation regime of the BT

302 Detailed meso- and microstructural analyses have unravelled the tectonic history of two different sectors (Area I
303 and Area II) of the BT in the Sardinian Variscan belt (Fig. 1b). This region has undergone a polyphase evolution

304 consisting of four ductile deformation phases. Sedimentary bedding S_0 is only observed in a few areas where a
305 strong lithological contrast is present. The D_1 structures are detectable far from the BT and mainly in the FW. The
306 S_1 foliation is defined by quartz + white mica + chlorite, indicating a greenschists-facies condition. The main
307 structures of the study area are controlled by the D_2 deformation phase. This phase is linked to the syn-nappe
308 stacking and exhumation of the HW (Carosi et al., 2004; Montomoli et al., 2018). We highlight an increase in
309 shear deformation along with the progressive transposition of previous D_1 structures approaching the BT. The
310 observed deformation gradient in Area I appears strikingly similar to that reported along the BT in the Area II
311 (Carosi et al., 2004; Montomoli et al., 2018). The S_2 foliation, parallel to the boundaries of the shear zone, and the
312 F_2 fold axes, perpendicular to the L_2 object lineation, are coeval with the overthrust of the Internal Nappe Zone
313 onto the External Nappe Zone (Carosi et al., 2004). The syn-kinematic mineral assemblage (chlorite + white mica)
314 along the S_2 mylonitic foliation is indicative of greenschist-facies metamorphic conditions. This is in agreement
315 with the main dynamic recrystallization mechanism of quartz, indicative of temperature ranges $\sim 400\text{-}450\text{ }^\circ\text{C}$ (BLG
316 II and local SGR; Piazzolo and Passchier 2002; Stipp et al., 2002). These data are corroborated by the presence of
317 undulose extinction, local flame perthite, and brittle deformation in feldspar, indicating $\sim 400\text{-}500\text{ }^\circ\text{C}$ (Pryer, 1993).
318 The observed relationships between mineral assemblage growth and deformation and dynamic recrystallization
319 mechanisms are broadly consistent with those reported by Montomoli et al. (2018), but with some differences.
320 Whilst, the syn-kinematic minerals observed during the D_2 phase are the same as previous authors, the observed
321 quartz recrystallization mechanism indicates slightly higher temperatures of deformation. However, the lack of
322 Grain Boundary Migration (GBM) in quartz, as highlighted by Conti et al. (1998), Montomoli et al. (2018), and
323 this work, indicates that deformation probably did not exceed $\sim 500\text{ }^\circ\text{C}$. Kinematic indicators, both at the meso-
324 and microscale, in Area I and II, reveal a top-to-the S-SW sense of shear. This also agrees with the S-SW F_2 fold
325 vergence detailed by previous authors (Carosi, 2004; Carosi et al., 2004; Montomoli et al., 2018). The whole
326 architecture of the Nappe Zone is affected by regional-scale F_3 folds (D_3). The D_3 phase is characterized by
327 pressure solution, indicating an upper structural level deformation. Also, the presence of the BT mylonitic zone in
328 the different sectors of the Barbagia Synform, with the same structural and kinematic features, indicates that F_3
329 folding deformed this tectonic contact. Similar structural results and the same shear sense were obtained from both

330 zones, confirming the post-nappe stacking folded structure (i.e., Barbagia Synform). Subsequent post-collision
331 extensional tectonics was characterized by the development of open folds (F_4).

332 *6.2. RSCM temperature variation along the BT*

333 Orogenic systems are partially characterized by successive and moderate overprinting thermal events (e.g., Brown,
334 1993; Delchini et al., 2016; Beyssac et al., 2019). One of them is the progressive increase of temperature along
335 shear zones (Thigpen et al., 2010). There are several methods for investigating the thermal architecture of a low-
336 temperature portion of orogenic belt, including vitrinite reflectance (Ferreiro Mählmann et al., 2012), illite and
337 chlorite crystallinity (Merriman et al., 1995; Jaboyedoff et al., 2001; Maino et al., 2015; Vidal et al., 2016), and
338 RSCM thermometry (Beyssac et al., 2002; Rahl et al., 2005; Aoya et al., 2010; Lahfid et al., 2010; Kouketsu et
339 al., 2014). Montomoli et al. (2018) performed both illite and chlorite crystallinity measurements on samples
340 transecting the BT, but found no systematic changes in those parameters across the structural profile. Compared
341 to the illite and chlorite crystallinity measurements, RSCM thermometer, in the absence of extreme fluid-rock
342 interaction or deformation (Moris-Muttoni et al., 2022 and references therein), may be more sensitive to the
343 temperature variation recording peak temperature (e.g., Beyssac et al., 2002; Lahfid et al., 2010; Aoya et al., 2010).
344 We document RSCM temperatures across the BT on both strongly deformed and weakly deformed samples taken
345 from two different structural sectors of the same shear zone. We highlight an increase in temperature moving from
346 the structurally higher parts of the HW, or from the structurally lower parts of the FW, toward the BT core. The
347 lowest RSCM temperature from non-mylonitic samples of both FW and HW (Fig. 11a, b) is slightly different in
348 Area I and II. Based on the geological framework, this T is linked to the maximum temperature reached during
349 collisional shortening and regional metamorphism in the HW and FW. RSCM temperatures range from ~420 to
350 ~450 °C, in agreement with the documented metamorphic mineral assemblage and recrystallization mechanism of
351 quartz and feldspar. In comparison, mylonites return higher RSCM temperatures ranging from ~470 to ~500 °C
352 (Fig. 10a). The detected RSCM T shift between non-mylonitic to mylonitic rocks is in the range of ~50-70 °C.

353 Several factors could cause this rise in temperature towards the core of shear zones: (i) graphite precipitation from
354 a hydrothermal fluid; (ii) detrital graphite; (iii) strain reorganization of graphite; and (iv) shear heating. Fluids

355 have previously been invoked to explain the presence of CM with unusual crystallinity (Skrzypek, 2021; Vitale
356 Brovarone et al., 2020). CM grains found in low-grade metamorphic rocks but indicating higher temperatures have
357 been explained by the precipitation of higher-crystallinity (lower R2) CM from hydrothermal fluids (Křibek et al.,
358 2008) or detrital origin (Galy et al., 2008). Whilst we cannot completely exclude fluid-rock interaction during
359 shear deformation or detrital origin of graphite, the presence of a systematic increase in the CM crystallinity from
360 the boundary to the core of the shear zone, in both areas, and the paucity of meso- and/or microscale evidence for
361 fluids (e.g., veins stockwork) make it to appear unlikely.

362 The RSCM data reported here show a persistent and systematic increase in T with increasing strain intensity
363 moving into the BT high strain shear zone. Several contributions have demonstrated that strain could reorganize
364 the structure of graphite (Kitamura et al., 2012; Furuichi et al., 2015; Kouketsu et al., 2019; Kedar et al., 2020;
365 Lyu et al., 2020; Nakamura et al., 2015, 2020). This strain-induced mechanism is similar to lattice modification
366 and recrystallization in the ductile deformation of minerals (Wang et al., 2019). If strain could reorganize the
367 structure of the CM, the obtained RSCM T may be not systematic in the temperature increase. However, the strain-
368 driven crystallization of CM is most effective in low-grade metamorphic rocks (~200-350 °C), where the
369 deformation could strongly modify the internal structure of CM (Wang et al., 2019). Our lowest temperatures have
370 been obtained from non-mylonitic samples and are associated with T of ~420-450 °C (Fig. 11a), linked to
371 collisional shortening and regional metamorphism. Thus, these samples are characterized by medium crystalline
372 and organized graphite that could be difficult to deform and give us an increase in temperature of ~50-70 °C due
373 to strain-induced mechanism. Despite this, we cannot completely exclude this factor.

374 Shear heating has been shown to produce temperature increases in shear zones (Molnar and England, 1990;
375 Camacho et al., 2001; Burg and Gerya, 2005; Mako and Caddick, 2018; Waters et al., 2018; Thigpen et al., 2021).

376 The amount of heat generated during shear heating varies as a result of several factors: (i) convergence rate, (ii)
377 strain rate, and (iii) width. Mako and Caddick (2018) used numerical models to calculate shear heating magnitudes
378 as high as ~200 °C, but they suggest that natural shear zones would probably produce much lower values. Thus,
379 several authors (Jamieson and Beaumont, 2013; Mako and Caddick, 2018; Waters et al., 2018; Iaccarino et al.,

2020) highlight that shear heating, in most common natural shear zones, produces relatively little heat compared to the surrounding rocks, probably on the order of $\sim 10\text{--}60$ °C. In particular, shear heating for low initial temperature ($\sim 300\text{--}400$ °C) is strongly dependent on convergence velocity (Waters et al., 2018). Shear heating >100 °C is only achievable with high convergence velocities ($\sim 3\text{--}5$ cm/year), whereas lower convergence velocities (~ 1 cm/year) can only produce heating >50 °C, according to the calculations of Mako and Caddick (2018). The strain rate and the width of the shear zone can also play an important role in the potential magnitudes of shear heating (Mako and Caddick, 2018). Integrating the strain rate values obtained by Montomoli et al. (2018) along the BT ($10^{-12}\text{--}10^{-14}$ s $^{-1}$) with the measured width of the shear zone in both transects (~ 600 m) in the Mako and Caddick (2018, their figure 9) graphs, it is possible to predict the potential temperature increase due to shear heating across the BT shear zone. Considering a shear activity ranging between 5-10 Ma and known strain rate values of Montomoli et al. (2018), for non-mylonitic rocks of initial temperature of $\sim 400\text{--}450$ °C, these integrated models of shear heating predict a T increase of ~ 50 °C. Moreover, the calculations of Mako and Caddick (2018) also imply that the observed maximum-T conditions are only possible for lower convergence velocities (≤ 3 cm/year). In summary, our RSCM T estimates derived both in Area I and II indicate that the temperature shift between the mylonitic and non-mylonitic rocks is approximately $\sim 50\text{--}70$ °C (Fig. 11a), in agreement with the numerical simulations. The displacement of the ductile shear zone is directly related to the strain rate, the width of the shear zone (Molnar and England, 1990; Waters et al., 2018), and the thermal architecture. The amount of erosion before the development of the BT is not known. However, temperatures of ~ 450 °C, obtained by the RSCM method in the HW metasediments imply depths of ~ 18 km when coupled with plausible thermal gradients of 25 °C km $^{-1}$ (Casini et al., 2012; Montomoli et al., 2018). In the above scenario, taking a thrust dip reference value of $\sim 35^\circ$, as roughly equivalent to the syn-orogenic dip of the BT, we can calculate the minimum magnitude of displacement of the BT. We obtain ~ 31 km of displacement (vertical depth/sin(thrust dip angle)), which may represent a first-order estimate for the minimum horizontal displacement on the BT. This result is confirmed by the distance calculated on the basis of cartographic evidence (estimated parallel to the shear plane) of about $\sim 20\text{--}30$ km, which is comparable to the amount reported by Carosi and Malfatti (1995). As highlighted by different

405 authors (Burg and Gerya, 2005; Waters et al., 2018), the fault displacement represents another important parameter
406 to be taken into account while discussing shear heating. Along shear zones with a considerable displacement, as
407 in this case, combined with a relatively short duration of ductile shearing, the most plausible heat source is shear
408 heating (Mako and Caddick, 2018). It is also worth noting that, even if the RSCM absolute error is about ± 50 °C
409 (Beysac et al., 2002, 2004), we detect a systematic thermal increase following the deformation gradient and
410 toward the BT in both Area I and II. Nevertheless, in the southernmost area, the thermal variation from non- to
411 strongly deformed rocks is larger than the absolute error of the method and thus increases the reliability of the
412 obtained data. However, the meaning of the detected thermal gradient across the BT is still uncertain.

413 Fluid circulation, strain reorganization and shear heating may be equally responsible for the increase in the
414 obtained RSCM temperatures. It is obvious that the driving factor strongly changes the interpretation of the
415 geological data. Nevertheless, due to the magnitude of the recorded increase in temperature that fits well with the
416 model predictions, the obtained results appear to be consistent with a shear heating model. A number of works
417 have documented that shear heating has strongly influenced the thermal structure of shear zones; as the Main
418 Central Thrust in the Himalayas (Molnar and England, 1990), the South Tibetan Detachment System in the Everest
419 region (Waters et al., 2018); for the Central and the Western Alps (Burg and Gerya, 2005; Schmalholz and Duretz,
420 2015); in the Davenport shear zone, central Australia (Camacho et al., 2001); the Norumbega fault zone, Central
421 Maine (Mako and Caddick, 2018); for the northern Scandian orogenic wedge (i.e., Moine, Ben Hope, Naver, and
422 Skinsdale Thrust; Thigpen et al., 2021) or for generic subduction zones (Peacock, 1992).

423 *6.3. Kinematics of the BT*

424 We define the deformation regime and the finite strain of the BT. The kinematic vorticity data obtained by the C'
425 shear bands method (Kurz and Northrup, 2008), PAR, and the RGN method (Jessup et al., 2007) have allowed
426 quantification of the flow regime as a non-coaxial flow. Concerning the uncertainties in the estimation of the
427 vorticity parameter, all methods, based on different assumptions, return consistent results from both Area I and II.
428 The object lineation within the BT is gently plunging and generally parallel to the dip of the main foliation, and
429 thus is compatible with a thrust-sense movement. Our data highlight that the component of the simple shear

430 increases progressively towards the centre of the BT, from both HW and FW rocks and in both Area I and II (Fig.
431 11b). We observe a general variation of simple shear from ~33% up to ~77%. Mylonites and less deformed rocks
432 record a flow regime dominated by pure shear, whereas ultramylonites in the center of the shear zone record an
433 increasing amount of simple shear. This is associated with a change of the finite strain ellipsoid, from close to the
434 plane strain up to prolate conditions.

435 Our results are in good agreement with the previous work on the BT. In fact, asymmetric F_2 folds observed in both
436 nappes with the axial plane parallel to the mylonitic foliation are linked to the BT non-coaxial deformation (Carosi
437 et al., 2004). According to the description by Fossen (2016), it is possible to suggest that the presence of this kind
438 of fold accommodates the component of shortening perpendicular to the BT. Contemporaneous pure and simple
439 shearing, due to the overthrust of the Internal Nappe Zone onto the External Nappe Zone, may explain the F_2 folds.
440 Finite strain data suggest a variation from general flattening to prolate ellipsoid, in agreement with an increase of
441 simple shear in thrust-sense shear zones (Vitale and Mazzoli, 2008; Fossen, 2016). A higher R_{xz} value is inferred
442 from ultramylonitic/within core samples compared to values from the other mylonitic samples, corroborating both
443 field and microstructural observations. This imply that the core of the BT accommodated a higher amount of strain
444 with respect to the shear zone peripheries (Fossen and Cavalcante, 2017). Higher W_k values, within the centre of
445 the BT, and a prolate strain ellipsoid are associated with higher RSCM T, whereas lower W_k values, far from the
446 BT core, and plane strain conditions are associated with samples showing lower RSCM T.

447 (insert Figure 11 here)

448 The progressive increase in temperature towards the BT, coupled with the increase of simple shear, could indicate
449 a syn-shearing temperature imprint. This broad correlation between RSCM T and the deformation gradient could
450 imply that the flow path was accompanied by a progressive localization of deformation in the core of the shear
451 zone, due to thermal weakening, during the ductile deformation (Vitale and Mazzoli, 2008). Although we lack
452 absolute timing constraints, these results fit well with the Type II shear zone growth model proposed by Fossen
453 and Cavalcante (2017). In this case, following the hypothesis of the shear heating model discussed above, the
454 deformation has been progressively localized in the central part of the shear zone due to thermal weakening. The

455 result, as in the here study case of the BT, is a shear zone with a deformation gradient increasing toward the centre
456 along with, associated to systematic variations in kinematic vorticity, finite strain and T based on RSCM (Fig. 12).

457 (insert Figure 12 here)

458 7. Conclusions

459 This study shows the importance of studying regional-scale shear zones with a multidisciplinary approach. We
460 provide quantitative constraints on deformation and peak temperature in two sectors of the BT (Fig. 12). The
461 strictly similar thermo-kinematic results and the same sense of shear obtained from two different sectors along the
462 BT (Area I and Area II) confirm the post-nappe stacking folded structure (i.e., Barbagia Synform) of the belt (Fig.
463 12). Valuable information can only be obtained if different and independent techniques are integrated to constrain
464 temperature and deformation in terms of peak temperature, finite strain, and kinematics of the flow. Detecting a
465 thermal gradient and, whenever possible, identifying the process that produces heating in a thrust-sense shear zone
466 in collisional systems is one of the primary results of this work. A combination of structural investigations at
467 different scales and of RSCM analyses reveals an increase in finite strain and of the simple shear component
468 coupled with the systematic increase in RSCM T, approaching the high-strain zone from the structurally higher
469 parts of the HW or from the structurally lower parts of the FW (Fig. 12). Regarding the nature of the heating, our
470 thermal results document that the paleothermal architecture of the BT best fits with a tectonic scenario of shear
471 heating. The heating quantified along the BT (~ 50 °C) is in agreement with the shear heating magnitudes calculated
472 by numerical and mechanical studies. By integrating different methodologies, we show that the BT represents a
473 major tectonic boundary that drove exhumation, divides the internal sector of the Sardinian orogenic wedge from
474 the external one, and represents a change from hinterland- to foreland-style deformation.

475 Acknowledgements

476 We want to thank Mutsuki Aoya and J. Ryan Thigpen for their constructive and thorough reviews. We thank
477 Fabrizio Agosta for his efficient editorial work. We also want to thank Jacob Forshaw for his useful suggestions.

478 References

- 479 Aoya, M., Kouketsu, Y., Endo, S., Shimizu, H., Mizukami, T., Nakamura, D., Wallis, S., 2010. Extending the
480 applicability of the Raman carbonaceous-material geothermometer using data from contact metamorphic rocks.
481 *Journal of Metamorphic Geology* 28, 95–914. <https://doi.org/10.1111/j.1525-1314.2010.00896.x>
- 482 Bailey, C.M., Polvi, L.E., Forte, A.M., 2007. Pure shear dominated high-strain zones in basement terranes.
483 *Geological Society American Memories* 200, 93-108.
- 484 Barca, S., Forci, A., Funedda, A., 2003. Nuovi dati stratigrafico-strutturali sul flysch ercinico dell'Unità del Gerrei
485 (Sardegna SE). In: Pascucci, V., (Ed.), *GeoSed*, Alghero 28-30 settembre 2003, 2003, 291–298, Sassari: University
486 of Sassari.
- 487 Bellanger, M., Augier, R., Bellahsen, N., Jolivet, L., Monié, P., Baudin, T., Beyssac, O., 2015. Shortening of the
488 European Dauphinois margin (Oisans Massif, Western Alps): new insights from RSCM maximum temperature
489 estimates and $40\text{Ar}/39\text{Ar}$ in situ dating. *Journal of Geodynamics* 83, 37–64.
490 <https://doi.org/10.1016/j.jog.2014.09.004>
- 491 Behr, W.M., Platt, J.P., 2014. Brittle faults are weak, yet the ductile middle crust is strong: implications for
492 lithospheric mechanics. *Geophysical Research Letters* 41, 8067-8075.
- 493 Beyssac, O., Lazzeri, M., 2012. Application of Raman spectroscopy to the study of graphitic carbons in the Earth
494 Sciences. In: Dubessy, J., Caumon, M.-C., Rull, F., *Raman spectroscopy applied to Earth sciences and cultural*
495 *heritage*, Mineralogical Society of Great Britain and Ireland 12, 415–454. [http://dx.doi.org/10.1180/emu-](http://dx.doi.org/10.1180/emu-notes.12.12)
496 [notes.12.12](http://dx.doi.org/10.1180/emu-notes.12.12)
- 497 Beyssac, O., Goffé, B., Chopin, C., Rouzaud, J. N., 2002. Raman spectra of carbonaceous material in
498 metasediments: a new geothermometer. *Journal of Metamorphic Geology* 20(9), 859–871.
499 <https://doi.org/10.1046/j.1525-1314.2002.00408.x>
- 500 Beyssac, O., Goffé, B., Petitet, J.-P., Froigneux, E., Moreau, M., Rouzaud, J.-N., 2003. On the characterization of
501 disordered and heterogeneous carbonaceous materials by Raman spectroscopy. *Spectrochimica Acta A* 59(10),
502 2267–2276. [https://doi.org/10.1016/S1386-1425\(03\)00070-2](https://doi.org/10.1016/S1386-1425(03)00070-2)
- 503 Beyssac, O., Bollinger, L., Avouac, J.P. Goffé, B., 2004. Thermal metamorphism in the lesser Himalaya of Nepal
504 determined from Raman spectroscopy of carbonaceous material. *Earth and Planetary Science Letters* 225, 233–
505 241. <https://doi.org/10.1016/j.epsl.2004.05.023>
- 506 Beyssac, O., Pattison, D.R.M., Bourdelle, F., 2019. Contrasting degrees of recrystallization of carbonaceous
507 material in the Nelson aureole, British Columbia and Ballachulish aureole, Scotland, with implications for
508 thermometry based on Raman spectroscopy of carbonaceous material. *Journal of Metamorphic Geology* 37, 71–
509 95. <https://doi.org/10.1111/jmg.12449>

- 510 Berger, A., Engi, M., Erne-Schmid, S., Glotzbach, C., Spiegel, C., de Goede, R., Herwegh, M., 2020. The relation
511 between peak metamorphic temperatures and subsequent cooling during continent–continent collision (western
512 Central Alps, Switzerland). *Swiss Journal of Geosciences* 113, 4. <https://doi.org/10.1186/s00015-020-00356-4>
- 513 Bollinger, L., Avouac, J. P., Beyssac, O., Catlos, E. J., Harrison, T. M., Grove, M., Goffé, B., Sapkota, S., 2004.
514 Thermal structure and exhumation history of the Lesser Himalaya in central Nepal. *Tectonics* 23(5), TC2015.
515 <https://doi.org/10.1029/2003TC001564>
- 516 Brown, M., 1993. P-T-t evolution of orogenic belts and the causes of regional metamorphism. *Journal of the*
517 *Geological Society* 150, 227–241.
- 518 Brun, J.-P., Cobbold, P.R., 1980. Strain heating and thermal softening in continental shear zones: a review. *Journal*
519 *of Structural Geology* 2, 149-158.
- 520 Burg, J.-P., Gerya, T.-V., 2005. The role of viscous heating in Barrovian metamorphism of collisional orogens:
521 Thermomechanical models and application to the Lepontine Dome in the Central Alps. *Journal of Metamorphic*
522 *Geology* 23, 75–95. <https://doi.org/10.1111/j.1525-1314.2005.00563.x>
- 523 Burg, J.-P., Schmalholz, S., 2008. Viscous heating allows thrusting to overcome crustalscale buckling: numerical
524 investigation with application to the Himalayan syntaxes. *Earth and Planetary Science Letters* 274 (1–2), 189–203.
525 <https://doi.org/10.1016/j.epsl.2008.07.022>
- 526 Calvino, F., 1959. Lineamenti strutturali del Sarrabus-Gerrei (Sardegna sud-orientale). *Bollettino del Servizio*
527 *Geologico d'Italia* 81(4–5), 489–556.
- 528 Camacho, A., McDougall, I., Armstrong, R., Braun, J., 2001. Evidence for shear heating, Musgrave Block, central
529 Australia. *Journal of Structural Geology* 23, 1007-1013.
- 530 Carmignani, L., Minzoni, N., Pertusati, P.C., Gattiglio, M., 1982. Lineamenti geologici principali del Sarcidano-
531 Barbagia di Belvì. In: Carmignani, L., Cocozza, T., Ghezzi, C., Pertusati, P.C., Ricci, C.A. (Ed.), *Guida alla*
532 *Geologia del Paleozoico Sardo. Guide Geologiche Regionali, Società Geologica Italiana*, 119–125.
- 533 Carmignani, L., Carosi, R., Di Pisa, A., Gattiglio, M., Musumeci, G., Oggiano, G., Pertusati, P.C., 1994. The
534 hercynian chain in Sardinia (Italy). *Geodinamica Acta* 7(1), 31–47.
535 <https://doi.org/10.1080/09853111.1994.11105257>
- 536 Carmignani, L., Oggiano, G., Barca, S., Conti, P., Eltrudis, A., Funedda, A., Pasci, S., Salvadori, I., 2001. *Geologia*
537 *della Sardegna (Note illustrative della Carta Geologica della Sardegna in scala 1:200.000). Memorie descrittive*
538 *della Carta Geologica d'Italia, Servizio Geologico Nazionale, Istituto Poligrafico e Zecca dello Stato, Roma.*

- 539 Carmignani, L., Oggiano, G., Funedda, A., Conti, P., Pasci, S., 2015. The geological map of Sardinia (Italy) at
540 1:250,000 scale. *Journal of Maps* 12(5), 826–835. <https://doi.org/10.1080/17445647.2015.1084544>
- 541 Carosi R., 2004. Carta geologico-strutturale del Monte S. Vittoria (Sarcidano-Barbagia di Belvì, Sardegna centrale,
542 Italia). Carosi, R., Elter, F.M., Gattiglio, M. (1997). Scala 1:25.000, Centrooffset, Siena, 1997. *Atti della Società*
543 *Toscana di Scienze Naturali serie A* 108 (2002-2003).
- 544 Carosi, R., Malfatti, G., 1995. Analisi Strutturale dell'Unità di Meana Sardo e caratteri della deformazione duttile
545 nel Sarcidano-Barbagia di Seulo (Sardegna centrale, Italia). *Atti della Società Toscana di Scienze Naturali, Serie*
546 *A* 102, 121–136.
- 547 Carosi, R., Pertusati, P.C., 1990. Evoluzione strutturale delle unità tettoniche erciniche nella Sardegna centro-
548 meridionale. *Bollettino della Società Geologica Italiana* 109, 325–335.
- 549 Carosi, R., Iacopini, D., Montomoli, C., 2004. Asymmetric folds development in the Variscan Nappe of central
550 Sardinia (Italy). *Comptes Rendus Geoscience* 336(10), 939–949. <https://doi.org/10.1016/j.crte.2004.03.004>
- 551 Carosi, R., Leoni, L., Paolucci, F., Pertusati, P.C., Trumpy, E., 2010. Deformation and illite crystallinity in
552 metapelitic rocks from the Mandas area, in the Nappe Zone of the Variscan belt of Sardinia; *Rendiconti Online*
553 *Società Geologica Italiana* 11, 393–394.
- 554 Carosi, R., Montomoli, C., Iacopini, D., 2002. Le pieghe asimmetriche dell'Unità di Meana Sardo, Sardegna
555 centrale (Italia): evoluzione e meccanismi di piegamento. *Atti della Società Toscana di Scienze Naturali, Serie A*
556 *108*, 51–58.
- 557 Carosi, R.; Montomoli, C.; Tiepolo, M.; Frassi, C. Geochronological constraints on post-collisional shear zones in
558 the Variscides of Sardinia (Italy). *Terra Nov.* 2012, 24, 42–51. <https://doi.org/10.1111/j.1365-3121.2011.01035.x>
- 559 Carosi, R., Musumeci, G., Pertusati, P.C., 1991. Differences in the structural evolution of tectonic units in central-
560 southern Sardinia. *Bollettino della Società Geologica Italiana* 110(3-4), 543–551.
- 561 Carosi, R., Petroccia, A., Iaccarino, S., Simonetti, M., Langone, A., Montomoli, C., 2020. Kinematics and timing
562 constraints in a transpressive tectonic regime: the example of the Posada-Asinara shear zone (NE Sardinia, Italy).
563 *Geosciences* 10, 288. <https://doi.org/10.3390/geosciences10080288>
- 564 Casini, L., Cuccuru, S., Maino, M., Oggiano, G., Tiepolo, M., 2012. Emplacement of the Arzachena Pluton
565 (Corsica-Sardinia Batholith) and the geodynamics of incoming Pangaea. *Tectonophysics* 544–545, 31–49.
566 <https://doi.org/10.1016/j.tecto.2012.03.028>
- 567 Casini, L., Funedda, A., Oggiano, G., 2010. A balanced foreland-hinterland deformation model for the Southern
568 Variscan belt of Sardinia, Italy. *Geological Journal* 45(5-6), 634–649. <https://doi.org/10.1002/gj.1208>

- 569 Chen, C.-T., Chan, Y.-C., Lu, C.-Y., Simoes, M., Beyssac, O., 2011. Nappe structure revealed by thermal
570 constraints in the Taiwan metamorphic belt. *Terra Nova* 23, 85-91. <https://doi.org/10.1111/j.1365-3121.2011.00987.x>
- 572 Cocco, F., Funedda, A., 2011. New data on the pre-Middle Ordovician deformation in SE Sardinia: a preliminary
573 note. *Rendiconti online della Società Geologica Italiana* 15, 34–36.
- 574 Cocco, F., Funedda, A., 2017. The Sardic phase: field evidence of Ordovician tectonics in SE Sardinia, Italy.
575 *Geological Magazine*, 1–14, <https://doi.org/10.1017/s0016756817000723>
- 576 Cocco, F., Oggiano, G., Funedda, A., Loi, A., Casini, L., 2018. Stratigraphic, magmatic and structural features of
577 Ordovician tectonics in Sardinia (Italy): a review. *Journal of Iberian Geology* 44, 619–639.
578 <https://doi.org/10.1007/s41513-018-0075-1>
- 579 Conti, P., Patta, E., 1998. Large scale Hercynian W-directed tectonics in southeastern Sardinia (Italy).
580 *Geodinamica Acta* 11(5), 217–231.
- 581 Conti, P., Funedda, A., Cerbai, N., 1998. Mylonite development in the Hercynian basement of Sardinia (Italy).
582 *Journal of Structural Geology* 20(2/3), 121–133. [https://doi.org/10.1016/S0191-8141\(97\)00091-6](https://doi.org/10.1016/S0191-8141(97)00091-6)
- 583 Conti, P., Carmignani, L., Cerbai, N., Eltrudis, A., Funedda, A., Oggiano, G., 1999. From thickening to extension
584 in the Variscan belt - kinematic evidence from Sardinia (Italy). *Terra Nova* 11(2/3), 93–99,
585 <https://doi.org/10.1046/j.1365-3121.1999.00231.x>
- 586 Conti, P., Carmignani, L., Funedda, A., 2001. Change of nappe transport direction during the Variscan collisional
587 evolution of central-southern Sardinia (Italy). *Tectonophysics* 332(1–2), 255–273, [https://doi.org/10.1016/S0040-1951\(00\)00260-2](https://doi.org/10.1016/S0040-1951(00)00260-2)
- 589 Coward, M.P., Kim, J.H., 1981. Strain within thrust sheets. In: McClay, K.R., Price, N.J. (Eds.), *Thrust and Nappe*
590 *Tectonics*. Geological Society of London Special Publication 9, 275-292.
- 591 Cruciani, G., Montomoli, C., Carosi, R., Franceschelli, M., Puxeddu, M., 2015. Continental collision from two
592 perspectives: a review of Variscan metamorphism and deformation in northern Sardinia. *Periodico di Mineralogia*
593 84, 3B, 657–699.
- 594 Dahlen, F.A., Suppe, J., Davis, D., 1984. Mechanics of fold-and-thrust belts and accretionary wedges — cohesive
595 Coulomb theory. *Journal of Geophysical Research* 89, 87–101.
- 596 Del Moro, A., Di Simplicio, P., Ghezzi, C., Guasparri, G., Rita, F., Sabatini, G., 1975. Radiometric data and
597 intrusive sequence in the Sardinian batholith. *Neues Jahrbuch für Mineralogie Monatshefte* 126, 28–44.

- 598 Delchini, S., Lahfid, A., Plunder, A., Michard, A., 2016. Applicability of the RSCM geothermometry approach in
599 a complex tectono-metamorphic context: The Jebilet massif case study (Variscan Belt, Morocco). *Lithos* 256–257,
600 1–12. <https://doi.org/10.1016/j.lithos.2016.04.007>
- 601 Dessau, G., Duchi, G., Moretti, A., Oggiano, G., 1982. Geologia della zona del Valico di Correboi (Sardegna
602 centro-orientale). Rilevamento, tettonica e giacimenti minerali. *Bollettino della Società Geologica Italiana* 101,
603 223–231.
- 604 Di Vincenzo, G., Carosi, R., Palmeri, R., 2004. The relationship between tectono-metamorphic evolution and
605 argon isotope records in white mica: Constraints from in situ ^{40}Ar - ^{39}Ar laser analysis of the Variscan basement
606 of Sardinia. *Journal of Petrology* 45, 1013–1043. <https://doi.org/10.1093/petrology/egh002>
- 607 Duretz, T., Schmalholz, S., Podladchikov, Y., Yuen, D., 2014. Physics-controlled thickness of shear zones caused
608 by viscous heating: implications for crustal shear localization. *Geophysical Research Letters* 41 (14), 4904–4911
- 609 Elliott, D., 1976. Motion of thrust sheets. *Geophysical Research Letters* 81, 949–963.
- 610 Fauconnier, J., Labrousse, L., Andersen, T.B., Beyssac, O., Duprat-Oualid, S., Yamato, P., 2014. Thermal
611 structure of a major crustal shear zone, the basal thrust in the Scandinavian Caledonides, *Earth and Planetary
612 Science Letters* 385, 162–171. <https://doi.org/10.1016/j.epsl.2013.10.038>
- 613 Ferreiro Mählmann, R., Bozkaya, Ö., Potel, S., Le Bayon, R., Šegvić, B., Nieto, F., 2012. The pioneer work of
614 Bernard Kübler and Martin Frey in very low-grade metamorphic terranes: paleo-geothermal potential of variation
615 in Kübler-index/organic matter reflectance correlations. A review. *Swiss Journal of Geosciences* 105, 121–152.
- 616 Flinn, D., 1962. On folding during three-dimensional progressive deformation. *The Quarterly journal of the
617 Geological Society of London* 118, 385–433
- 618 Fossen, H., 2016. *Structural Geology*, second ed. Cambridge University Press, Cambridge, United Kingdom.
- 619 Fossen, H., Cavalcante, G.C.G., 2017. Shear zones – a review. *Earth-Science Reviews* 171, 434–455.
620 <https://doi.org/10.1016/j.earscirev.2017.05.002>
- 621 Franceschelli, M., Gattiglio, M., Pannuti, F., Fadda, S., 1992. Illite crystallinity in pelitic rocks from the external
622 and nappe zones of the Hercynian chain of Sardinia. In: Carmignani, L., Sassi, F.P., (Ed.), *Contributions to the
623 Geology of Italy with special regard to the Paleozoic Basements: IGCP Project No. 276, Newsletter* 127–135.
- 624 Franceschelli, M., Puxeddu, M., Cruciani, G., 2005. Variscan metamorphism in Sardinia, Italy: review and
625 discussion. *Journal of the Virtual Explorer* 19, 2. <http://dx.doi.org/10.3809%2Fjvirtex.2005.00121>
- 626 Fry, N., 1979. Random point distribution and strain measurement in rocks. *Tectonophysics* 60, 89–105.
627 [https://doi.org/10.1016/0040-1951\(79\)90135-5](https://doi.org/10.1016/0040-1951(79)90135-5)

- 628 Funedda, A., 2009. Foreland- and hinterland-verging structures in fold-and-thrust belt: an example from the
629 Variscan foreland of Sardinia. *International Journal of Earth Sciences* 98, 1625–1642,
630 <https://doi.org/10.1007/s00531-008-0327-y>
- 631 Funedda, A., Naitza, S., Conti, P., Dini, A., Butta, C., Tocco, S., Carmignani, L., 2011. The geological and
632 metallogenic map of the Baccu Locci mine area (Sardinia, Italy). *Journal of Maps* 7(1), 103–114.
633 <https://doi.org/10.4113/jom.2011.1134>
- 634 Funedda, A., Meloni, M.A., Loi, A., 2015. Geology of the Variscan basement of the Laconi-Asuni area (central
635 Sardinia, Italy): the core of a regional antiform refolding a tectonic nappe stack. *Journal of Maps* 11(1), 146–156.
636 <https://doi.org/10.1080/17445647.2014.942396>
- 637 Furuichi, H., Ujiie, K., Kouketsu, Y., Saito, T., Tsutsumi, A., Wallis, S., 2015. Vitrinite reflectance and Raman
638 spectra of carbonaceous material as indicators of frictional heating on faults: Constraints from friction experiments.
639 *Earth and Planetary Science Letters* 424, 191–200. <https://doi.org/10.1016/j.epsl.2015.05.037>
- 640 Galy, V., Beyssac, O., France-Lanord, C., and Eglinton, T. I, 2008 Recycling of graphite during Himalayan
641 erosion: A geological stabilization of carbon in the crust. *Science* 322, 943–945
642 <http://dx.doi.org/10.1126/science.1161408>
- 643 Ghosh, P., Bhattacharyya, K., Parui, C., 2020. Tracking progressive deformation of an orogenic wedge through
644 two successive internal thrusts: Insights from structure, deformation profile, strain, and vorticity of the Main
645 Central thrust (MCT) and the Pelling-Munsiari thrust (PT), Sikkim Himalayan fold thrust belt. *Journal of Structural*
646 *Geology* 140. <https://doi.org/10.1016/j.jsg.2020.104120>
- 647 Gillam, B.G., Little, T.A., Smith, E., Toy V.G., 2013. Extensional shear band development on the outer margin of
648 the Alpine mylonite zone, Tatare Stream, Southern Alps, New Zealand. *Journal of Structural Geology* 54, 1–20.
649 <https://doi.org/10.1016/j.jsg.2013.06.010>
- 650 Grasemann, B., Fritz, H., Vannay, J.C., 1999. Quantitative kinematic flow analysis from the Main Central Thrust
651 Zone (NW-Himalaya, India): implications for a decelerating strain path and the extrusion of orogenic wedges.
652 *Journal of Structural Geology* 21, 837–853. [https://doi.org/10.1016/s0191-8141\(99\)00077-2](https://doi.org/10.1016/s0191-8141(99)00077-2)
- 653 Grujic, D., Ashley, K. T., Coble, M. A., Coutand, I., Kellett, D. A., Larson, K. P., Whipp, D. M. Jr., Gao, M.,
654 Whynot, N., 2020. Deformational temperatures across the Lesser Himalayan Sequence in eastern Bhutan and their
655 implications for the deformation history of the Main Central Thrust. *Tectonics* 39, e2019TC005914.
656 <https://doi.org/10.1029/2019TC005914>

- 657 Handy, M., Hirth, G., Bürgmann, R., 2007. Continental fault structure and rheology from the frictional-to-viscous
658 transition downward. In: Handy, M., Hirth, G., Hovius, N. (Ed.), *Tectonic Faults: Agents of Change on a Dynamic*
659 *Earth*. The MIT Press., Cambridge, Mass.
- 660 Henry, D.G., Jarvis, I., Gillmore, G., Stephenson, M., 2019. Raman spectroscopy as a tool to determine the thermal
661 maturity of organic matter: Application to sedimentary, metamorphic and structural geology. *Earth-Science*
662 *Reviews* 198, 102936. <https://doi.org/10.1016/j.earscirev.2019.102936>
- 663 Hirth, G., Teyssier, C., Dunlap, W.J., 2001. An evaluation of quartzite flow laws based on comparisons between
664 experimentally and naturally deformed rocks. *International Journal of Earth Sciences* 90, 77–87
- 665 Iaccarino, S., Montomoli, C., Montemagni, C., Massonne, H. –J., Langone, A., Jain, A. K., Visona, D., Carosi, R.,
666 2020. The main central thrust zone along the Alaknanda and Dhaul Ganga valleys (Garhwal Himalaya, NW India):
667 Insights into an inverted metamorphic sequence. *Lithos* 372–373, 105669.
668 <https://doi.org/10.1016/j.lithos.2020.105669>
- 669 Iacopini, D., Frassi, C., Carosi, R., Montomoli, C., 2011. Biases in three-dimensional vorticity analysis using
670 porphyroclast system: Limits and application to natural examples. *Geological Society of London, Special*
671 *Publications* 360, 301–318. <https://doi.org/10.1144/SP360.17>
- 672 Jaboyedoff, M., Bussy, F., Kübler, B., Thelin, P., 2001. Illite “crystallinity” revisited. *Clay Minerals* 49, 156–167.
- 673 Jamieson, R.A., Beaumont, C., 2013. On the origin of orogens. *Geological Society of America Bulletin* 125, 1671–
674 1702. <https://doi.org/10.1130/B30855.1>
- 675 Jaquet, Y., Duretz, T., Grujic, D., Masson, H., Schmalholz, S. M., 2018. Formation of orogenic wedges and crustal
676 shear zones by thermal softening, associated topographic evolution and application to natural orogens.
677 *Tectonophysics* 746, 512–529. <https://doi.org/10.1016/j.tecto.2017.07.021>
- 678 Jessup, M. J., Law, R. J., Frassi, C., 2007. The Rigid Grain Net (RGN): An alternative method for estimating mean
679 kinematic vorticity number (Wm). *Journal of Structural Geology* 29,411–421.
680 <https://doi.org/10.1016/j.jsg.2006.11.003>
- 681 Kaneki, S., Hirono, T., Mukoyoshi, H., Sampei, Y., Ikehara, M., 2016. Organochemical characteristics of
682 carbonaceous materials as indicators of heat recorded on an ancient plate-subduction fault, *Geochemistry,*
683 *Geochemistry, Geophysics, Geosystems* 17(7), 2855–2868, [doi:10.1002/2016GC006368](https://doi.org/10.1002/2016GC006368)
- 684 Kedar, L., Bond, C., Muirhead, D., 2020. Carbon ordering in an aseismic shear zone: implications for crustal
685 weakening and Raman spectroscopy. *EGU General Assembly 2020, Online*, 4–8 May 2020, EGU2020-9155.
686 <https://doi.org/10.5194/egusphere-egu2020-9155>

- 687 Kitamura, M., Mukoyoshi, H., Fulton, P.M., Hirose, T., 2012. Coal maturation by frictional heat during rapid
688 fault slip. *Geophysical Research Letters* 39, 1–5. <https://doi.org/10.1029/2012gl052316>
- 689 Kouketsu, Y., Miyake, A., Igami, Y., Taguchi, T., Kagi, H., Enami, M., 2019. Drastic effect of shearing on graphite
690 microtexture: attention and application to Earth science. *Prog. Earth and Planetary Science Letters* 6, 23.
691 <https://doi.org/10.1186/s40645-019-0271-4>
- 692 Kouketsu, Y., Mizukami, T., Mori, H., Endo, S., Aoya, M., Hara, H., Nakamura, D., Wallis, S., 2014. Raman CM
693 geothermometer using FWHM. *Island Arc* 23, 33–50. <https://doi.org/10.1111/iar.12057>
- 694 Kříbek, B., Sýkorová, I., Machovič, V., Laufek, F., 2008. Graphitization of organic matter and fluid-deposited
695 graphite in Palaeoproterozoic (Birimian) black shales of the Kaya-Goren greenstone belt (Burkina Faso, West
696 Africa). *Journal of Metamorphic Geology* 26, 937–958. <https://doi.org/10.1111/j.1525-1314.2008.00796.x>
- 697 Kuo, L.-W., Di Felice, F., Spagnuolo, E., Di Toro, G., Song, S.-R., Aretusini, S., Li, H., Suppe, J., Si, J., Wen, C.-
698 Y., 2017. Fault gouge graphitization as evidence of past seismic slip. *Geology* 45 (11),979–982.
699 <https://doi.org/10.1130/G39295.1>
- 700 Kuo L.W., Huang, J.R., Fang, J.N., Si, J., Song, S.R., Li, H., Yeh, E.C., 2018. Carbonaceous materials in the fault
701 zone of the longmenshan fault belt: 2. characterization of fault gouge from deep drilling and implications for fault
702 maturity. *Minerals* 8(9), 393. <https://doi.org/10.3390/min8100457>
- 703 Kurz, G.A., Northrup, C.J., 2008. Structural analysis of mylonitic fault rocks in the Cougar Creek Complex,
704 Oregon-Idaho using the porphyroclast hyperbolic distribution method, and potential use of sc'-type extensional
705 shear bands as quantitative vorticity indicators. *Journal of Structural Geology* 30, 1005–1012.
706 <https://doi.org/10.1016/j.jsg.2008.04.003>
- 707 Lahfid, A., Beyssac, O., Deville, E., Negro, F., Chopin, C., Goffé, B., 2010. Evolution of the Raman spectrum of
708 carbonaceous material in low-grade metasediments of the Glarus Alps (Switzerland). *Terra Nova* 22, 354–360.
709 <https://doi.org/10.1111/j.1365-3121.2010.00956.x>
- 710 Larson, K. P., Godin, L., Davis, W. J., Davis, D. W., 2010. Relationships between displacement and distortion in
711 orogens: Linking the Himalayan foreland and hinterland in central Nepal. *Geological Society of America Bulletin*
712 122, 1116–1134. <https://doi.org/10.1130/b30073.1>
- 713 Law, R.D., 2014. Deformation thermometry based on quartz c-axis fabrics and recrystallization microstructures:
714 A review. *Journal of Structural Geology* 66, 129–161. <https://doi.org/10.1016/j.jsg.2014.05.023>

- 715 Law, R.D., Searle, M.P., Simpson, R.L., 2004. Strain, deformation temperatures and vorticity of flow at the top of
716 the Greater Himalayan Slab, Everest Massif, Tibet. *Journal of the Geological Society* 161, 305–320.
717 <https://doi.org/10.1144/0016-764903-047>
- 718 Law, R.D., Thigpen, J.R., Mazza, S.E., Mako, C.A., Krabbendam, M., Spencer, B.M., Ashley, K.T., Strachan,
719 R.A., Davis, E.F., 2021. Tectonic Transport Directions, Shear Senses and Deformation Temperatures Indicated by
720 Quartz c-Axis Fabrics and Microstructures in a NW-SE Transect across the Moine and Sgurr Beag Thrust Sheets,
721 Caledonian Orogen of Northern Scotland. *Geosciences* 11, 411. <https://doi.org/10.3390/geosciences11100411>
- 722 Lyu, M., Cao, S., Neubauer, F., Xuemei Cheng, J.L., 2020. Deformation fabrics and strain localization mechanisms
723 in graphitic carbon-bearing rocks from the Ailaoshan-Red River strike-slip fault zone. *Journal of Structural*
724 *Geology* 140. <https://doi.org/10.1016/j.jsg.2020.104150>
- 725 Maino, M., Casini, L., Ceriani, A., Decarlis, A., Di Giulio, A., Seno, S., Setti, M., Stuart, F., 2015. Dating shallow
726 thrusts with zircon (U-Th)/ He thermochronometry - The shear heating connection. *Geology* 43(6), 495-498.
727 <https://doi.org/10.1130/G36492.1>
- 728 Mako, C.A., Caddick, M.J., 2018. Quantifying magnitudes of shear heating in metamorphic systems.
729 *Tectonophysics* 744, 499–517. <https://doi.org/10.1016/j.tecto.2018.07.003>
- 730 Malavieille, J., Dominguez, S., Lu, C.-Y., Chen, C.-T., Konstantinovskaya., E., 2019. Deformation partitioning in
731 mountain belts: insights from analogue modelling experiments and the Taiwan collisional orogen. *Geological*
732 *Magazine* 158(1), 1-20. <https://doi.org/10.1017/S0016756819000645>
- 733 Matte, P., 2001. The Variscan collage and orogeny (480–290 ma) and the tectonic definition of the Armorica
734 microplate: A review. *Terra Nova* 13, 117–121. <https://doi.org/10.1046/j.1365-3121.2001.00327.x>
- 735 Merriman, R.J., Roberts, B., Peacor, D.R., Hirons, S.R., 1995. Strain-related differences in the crystal growth of
736 white mica and chlorite: a TEM and XRD study of development of pelite microfabrics in the Southern Uplands
737 thrust terrane, Scotland. *Journal of Metamorphic Geology* 13, 559-576.
- 738 Mitra, G., 1994. Strain variation in thrust sheets across the Sevier fold-and-thrust belt (Idaho- Utah-Wyoming):
739 implications for section restoration and wedge taper evolution. *Journal of Structural Geology* 16, 585e602.
- 740 Molli, G., Vitale Brovarone, A., Beyssac, O., Cinquini, I., 2018. RSCM thermometry in the Alpi Apuane (NW
741 Tuscany, Italy): New constraints for the metamorphic and tectonic history of the inner northern Apennines. *Journal*
742 *of Structural Geology* 113, 200–216. <https://doi.org/10.1016/j.jsg.2018.05.020>.
- 743 Molnar, P., England, P., 1990. Temperatures, heat flux, and frictional stress near major thrust faults. *Journal of*
744 *Geophysical Research* 95, 4833. <https://doi.org/10.1029/JB095iB04p04833>.

- 745 Montési, L.G.J., 2013. Fabric development as the key for forming ductile shear zones and enabling plate tectonics.
746 *Journal of Structural Geology* 50, 254–266. <https://doi.org/10.1016/j.jsg.2012.12.011>
- 747 Montési, L.G.J., Zuber, M.T., 2002. A unified description of localization for application to large-scale tectonics.
748 *Journal of Geophysical Research* 107 (B3), 1–21. <https://doi.org/10.1029/2001JB000465>
- 749 Montmartin, C., Faure, M., Raimbourg, H., 2021. Paleotemperature investigation of the Variscan southern external
750 domain: the case of the Montagne Noire (France). *BSGF - Earth Sciences Bulletin* 192 :3
751 <http://dx.doi.org/10.1051/bsgf/2020043>
- 752 Montomoli, C., 2003. Zone di taglio fragili-duttile nel basamento varisco metamorfico di basso grado della Nurra
753 meridionale (Sardegna nord-occidentale). *Atti della Società Toscana di Scienze Naturali, Serie A* 108, 23–29.
- 754 Montomoli, C., Iaccarino, S., Simonetti, M., Lezzerini, M., Carosi, R., 2018. Structural setting, kinematics and
755 metamorphism in a km-scale shear zone in the inner nappes of Sardinia (Italy). *Italian Journal of Geosciences* 137,
756 294–310. <https://doi.org/10.3301/IJG.2018.16>
- 757 Mori, H., Mori, N., Wallis, S., Westaway, R., Annen, C., 2017. The importance of heating duration for Raman
758 CM thermometry: evidence from contact metamorphism around the Great Whin Sill intrusion, UK. *Journal of*
759 *Metamorphic Geology* 35, 165-180. <https://doi.org/10.1111/jmg.12225>
- 760 Moris-Muttoni, B., Raimbourg, H., Augier, R., Champallier, R., LeTrong, E., 2022. The impact of melt versus
761 mechanical wear on the formation of pseudotachylite veins in accretionary complexes. *Scientific Reports* 12,
762 1529. <https://doi.org/10.1038/s41598-022-05379-5>
- 763 Muirhead, D. K., Kedar, L., Schito, A., Corrado, S., Bond, C. E., Romano, C., 2021. Raman spectral shifts in
764 naturally faulted rocks. *Geochemistry, Geophysics, Geosystems*, 22, e2021GC009923.
765 <https://doi.org/10.1029/2021GC009923>
- 766 Musumeci, G., 1992. Ductile wrench tectonics and exhumation of hercynian metamorphic basement in Sardinia:
767 Monte Grighini Complex. *Geodinamica Acta* 5(1-2), 119-133
- 768 Nakamura, Y., Oohashi, K., Toyoshima, T., Satish-Kumar, M., Akai, J., 2015. Strain-induced amorphization of
769 graphite in fault zones of the Hidaka metamorphic belt, Hokkaido, Japan. *Journal of Structural Geology* 72, 142–
770 161. <https://doi.org/10.1016/j.jsg.2014.10.012>
- 771 Nakamura, Y., Yoshino, T., Satish-Kumar, M., 2017. An experimental kinetic study on the structural evolution of
772 natural carbonaceous material to graphite. *American Mineralogist* 102, 135–148. [https://doi.org/10.2138/am-](https://doi.org/10.2138/am-2017-5733)
773 [2017-5733](https://doi.org/10.2138/am-2017-5733)

- 774 Nakamura, Y., Yoshino, T., Satish-Kumar, M., 2020. Pressure dependence of graphitization: implications for rapid
775 recrystallization of carbonaceous material in a subduction zone. *Contributions to Mineralogy and Petrology* 175,
776 32. <https://doi.org/10.1007/s00410-020-1667-2>
- 777 Nibourel, L., Berger, A., Egli, D., Heuberger, S., Herwegh, M., 2021. Structural and thermal evolution of the
778 eastern Aar Massif: insights from structural field work and Raman thermometry. *Swiss Journal of Geosciences*
779 114, 9. <https://doi.org/10.1186/s00015-020-00381-3>
- 780 Passchier, C.W., 1987. Stable positions of rigid objects in non-coaxial flow—a study in vorticity analysis. *Journal*
781 *of Structural Geology* 9, 679 – 690. [https://doi.org/10.1016/0191-8141\(87\)90152-0](https://doi.org/10.1016/0191-8141(87)90152-0)
- 782 Passchier, C.W., Trouw, R. A. J., 2005. *Microtectonics*. Springer, Berlin, Heidelberg. [https://doi.org/10.1007/3-](https://doi.org/10.1007/3-540-29359-0)
783 [540-29359-0](https://doi.org/10.1007/3-540-29359-0)
- 784 Pavanetto, P., Funedda, A., Northrup, C.J., Schmitz, M., Crowley, J., Loi, A., 2012. Structure and U-Pb zircon
785 geochronology in the Variscan foreland of SW Sardinia, Italy. *Geological Journal* 47(4), 426–455.
786 <http://dx.doi.org/10.1002%2Fgj.1350>
- 787 Peacock, S.M., 1992. Blueschist-facies metamorphism, shear heating, and P-T-t paths in subduction shear zones.
788 *Journal of Geophysical Research* 97.
- 789 Perez-Caceres, I., Martinez Poyatos, D.J., Vidal, O., Beyssac, O., Nieto, F., Simancas, J.F., Azor, A., Bourdelle,
790 F., 2020. Deciphering the Metamorphic Evolution of the Pulo Do Lobo Metasedimentary Domain (SW Iberian
791 Variscides). *Solid Earth* 11, 469–488. <https://doi.org/10.5194/se-11-469-2020>
- 792 Pertusati, P., Sarria, E., Cherchi, G.P., Carmignani, L., Barca, S., Benedetti, M., Chighine, G., Cincotti, F.,
793 Oggiano, G., Ulzega, A., Orrù, P., Pintus, C., 2002. Note illustrative della Carta Geologica d'Italia alla scala
794 1:50.000 - foglio 541 Jerzu, pp. 143, Servizio Geologico D'Italia.
- 795 Piazzolo, S., Passchier, C.W., 2002. Controls on lineation development in low to medium grade shear zones: a study
796 from the Cap de Creus peninsula, NE Spain. *Journal of Structural Geology* 24(1), 25–44.
797 [https://doi.org/10.1016/S0191-8141\(01\)00045-1](https://doi.org/10.1016/S0191-8141(01)00045-1)
- 798 Platt, J.P., 1986. Dynamics of orogenic wedges and the uplift of high-pressure metamorphic rocks. *Geological*
799 *Society of America Bulletin* 97 (9), 1037–1053.
- 800 Platt, J., 1993. Exhumation of high-pressure rocks: a review of concepts and processes. *Terra Nova* 5 (2), 119–
801 133.
- 802 Platt, J.P., 2015. Rheology of two-phase systems: a microphysical and observational approach. *Journal of*
803 *Structural Geology* 77, 213-227.

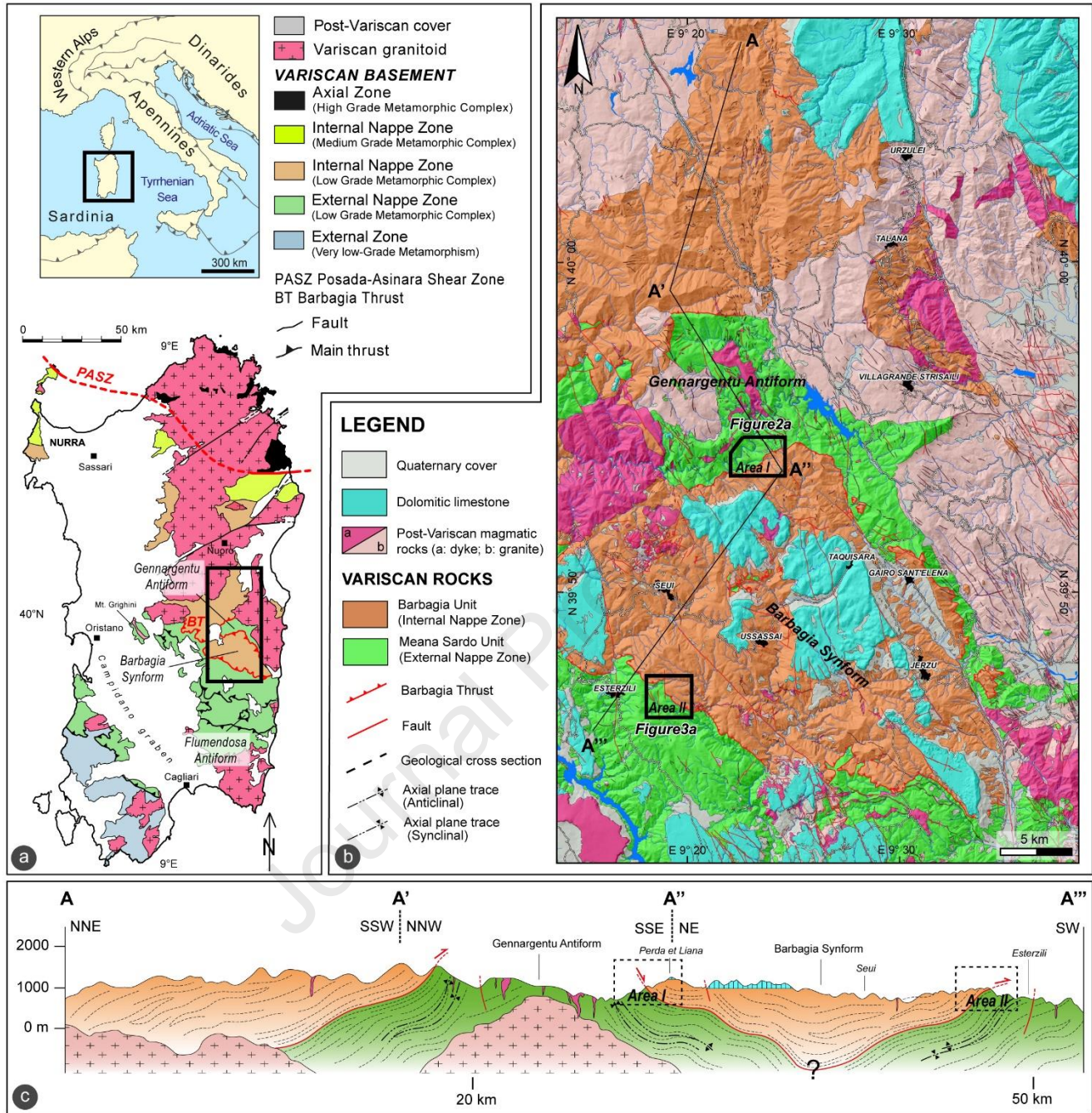
- 804 Platt, J.P., 2018. Corrigendum to “Influence of shear heating on microstructurally defined plate boundary shear
805 zones” [2015, *Journal of Structural Geology*, 79, 80-89]. *Journal of Structural Geology* 113, 242–243.
806 <https://doi.org/10.1016/j.jsg.2017.08.005>
- 807 Platt, J.P., Behr, W.M., 2011. Grainsize evolution in ductile shear zones: Implications for strain localization and
808 the strength of the lithosphere. *Journal of Structural Geology* 33, 537e550.
809 <http://dx.doi.org/10.1016/j.jsg.2011.01.018>
- 810 Platt, J.P., Vissers, R.L.M., 1980. Extensional structures in anisotropic rocks. *Journal of Structural Geology* 2,
811 397–410
- 812 Pryer, L.L., 1993. Microstructures in feldspars from a major crustal thrust zone: The Greenville Front, Ontario,
813 Canada. *Journal of Structural Geology* 15, 21–36. [https://doi.org/10.1016/0191-8141\(93\)90076-M](https://doi.org/10.1016/0191-8141(93)90076-M)
- 814 Ramsay, J. G., 1967. *Folding and fracturing of rocks* McGraw-Hill.
- 815 Rahl, J.M., Anderson, K.M., Brandon, M.T., Fassoulas, C., 2005. Raman spectroscopic carbonaceous material
816 thermometry of lowgrade metamorphic rocks: Calibration and application to tectonic exhumation in Crete, Greece.
817 *Earth and Planetary Science Letters* 240, 339–354. <https://doi.org/10.1016/j.epsl.2005.09.055>
- 818 Rantitsch, G., Iglseder, C., Schuster, R., Hollinetz, M. S., Huet, B., Werdenich, M., 2020. Organic metamorphism
819 as a key for reconstructing tectonic processes: a case study from the Austroalpine unit (Eastern Alps). *International*
820 *Journal of Earth Sciences* 109, 2235–2253. <https://doi.org/10.1007/s00531-020-01897-7>
- 821 Regenauer-Lieb, K., Rosenbaum, G., Lyakhovsky, V., Liu, J., Weinberg, R., Segev, A., Weinstein, Y., 2015. Melt
822 instabilities in an intraplate lithosphere and implications for volcanism in the Harrat Ash-Shaam volcanic field
823 (NW Arabia). *Journal of Geophysical Research* 120 (3), 1543–1558. <https://doi.org/10.1002/2014JB011403>
- 824 Ring, U., Brandon, M.T., 1999. Ductile deformation and mass loss in the Franciscan Subduction complex:
825 implications for exhumation processes in accretionary wedges. In: Ring, U., Brandon, M.T., Lister, G.S., Willett,
826 S.D. (Ed.), *Exhumation Processes: Normal Faulting, Ductile Flow and Erosion*. Geological Society of London
827 Special Publication 154, 55-86.
- 828 Ring, U., Kumerics, C., 2008. Vertical ductile thinning and its contribution to the exhumation of high-pressure
829 rocks: the Cycladic blueschist unit in the Aegean. *Journal of the Geological Society* 165, 1019-1030.
- 830 Ring, U., Bernet, M., Tulloch, A., 2015. Kinematic, finite strain and vorticity analysis of the Sisters shear zone,
831 Stewart Island, New Zealand. *Journal of Structural Geology* 73, 114-129

- 832 Ring, U., Brandon, M.T., Ramthun, A., 2001. Solution-mass-transfer deformation adjacent to the Glarus Thrust,
833 with implications for the tectonic evolution of the Alpine wedge in eastern Switzerland. *Journal of Structural*
834 *Geology* 23, 1491–1505. [https://doi.org/10.1016/S0191-8141\(01\)00015-3](https://doi.org/10.1016/S0191-8141(01)00015-3)
- 835 Sanderson, D.J., 1982. Models of strain variation in nappes and thrust sheets: a review. *Tectonophysics* 88, 201-
836 233.
- 837 Scharf, A., Handy, M.R., Ziemann, M.A., Schmid, S.M., 2013. Peak-temperature patterns of polyphase
838 metamorphism resulting from accretion, subduction and collision (eastern Tauern window, European alps) – a
839 study with Raman microspectroscopy on carbonaceous material (RSCM). *Journal of Metamorphic Geology* 31,
840 863–880. <https://doi.org/10.1111/jmg.12048>
- 841 Schmalholz, S., Duretz, T., 2015. Shear zone and nappe formation by thermal softening, related stress and
842 temperature evolution, and application to the Alps. *Journal of Metamorphic Geology* 33(8), 887–908.
843 <https://doi.org/10.1111/jmg.12137>
- 844 Schneider, J., Corsini, M., Peila, A., Lardeaux, J., 2014. Thermal and mechanical evolution of an orogenic wedge
845 during Variscan collision: an example in the Maures-Tanneron Massif (SE France). *Geological Society of London*
846 405, 313-331. <https://doi.org/10.1144/SP405.4>
- 847 Schott, B., Yuen, D., Schmeling, H., 2000. The significance of shear heating in continental delamination. *Physics*
848 *of the Earth and Planetary Interiors* 118, 273-290.
- 849 Seno, S., Dallagiovanna, G., Vanossi, M., 1998. From finite strain data to strain history: a model for a sector of
850 the Ligurian Alps, Italy. *Journal of Structural Geology* 20, 573-585. [https://doi.org/10.1016/S0191-](https://doi.org/10.1016/S0191-8141(97)00104-1)
851 [8141\(97\)00104-1](https://doi.org/10.1016/S0191-8141(97)00104-1)
- 852 Simonetti, M., Carosi, R., Montomoli, C., Cottle, J.M., Law, R.D., 2020a. Transpressive deformation in the
853 southern European variscan belt: new insights from the Aiguilles Rouges massif (western Alps). *Tectonics* 39.
854 <https://doi.org/10.1029/2020TC006153>
- 855 Simonetti, M., Carosi, R., Montomoli, C., Corsini, M., Petroccia, A., Cottle, J.M., Iaccarino, S., 2020b. Timing
856 and kinematics of flow in a transpressive dextral shear zone, Maures Massif (Southern France). *International*
857 *Journal of Earth Sciences* 109, 2261–2285. <https://doi.org/10.1007/s00531-020-01898-6>
- 858 Simonetti, M., Carosi, R., Montomoli, C., Law, R.D., Cottle, J.M., 2021. Unravelling the development of regional-
859 scale shear zones by a multidisciplinary approach: The case study of the Ferriere-Mollières Shear Zone (Argentera
860 Massif, Western Alps). *Journal of Structural Geology* 149, 104399. <https://doi.org/10.1016/j.jsg.2021.104399>.

- 861 Simpson, C. De Paor, D.G., 1993. Strain and kinematic analysis in general shear zones. *Journal of Structural*
862 *Geology* 15, 1–20. [https://doi.org/10.1016/0191-8141\(93\)90075-1](https://doi.org/10.1016/0191-8141(93)90075-1)
- 863 Skrzypek, E., 2021. First- and second-order Raman spectra of carbonaceous material through successive contact
864 and regional metamorphic events (Ryoke belt, SW Japan). *Lithos* 388-389, 106029.
865 <https://doi.org/10.1016/j.lithos.2021.106029>.
- 866 Steck, A., 2008. Tectonics of the Simplon massif and Lepontine gneiss dome: deformation structures due to
867 collision between the underthrusting European plate and the Adriatic indenter. *Swiss Journal of Geosciences* 101,
868 515–546. <https://doi.org/10.1007/s00015-008-1283-z>
- 869 Steck, A., Della Torre, F., Keller, F., Pfeifer, H.-R., Hunziker, J., Masson, H., 2013. Tectonics of the Lepontine
870 Alps: ductile thrusting and folding in the deepest tectonic levels of the Central Alps. *Swiss Journal of Geosciences*
871 106, 427–450. <https://doi.org/10.1007/s00015-013-0135-7>
- 872 Stipp, M., Stünitz, H., Heilbronner, R., Schmid, S.M., 2002. Dynamic recrystallization of quartz: correlation
873 between natural and experimental conditions. *Geological Society of London, Special Publications* 200, 171–190.
874 <https://doi.org/10.1144/GSL.SP.2001.200.01.11>
- 875 Takeuchi, C.S., Fialko, Y., 2012. Dynamic models of interseismic deformation and stress transfer from plate
876 motion to continental transform faults. *Journal of Geophysical Research* 117, B05403.
877 <https://doi.org/10.1029/2011JB009056>
- 878 Thielmann, M., Kaus, B.J.P., 2012. Shear heating induced lithospheric-scale localization: does it result in
879 subduction? *Earth and Planetary Science Letters* 359, 1-13. <https://doi.org/10.1016/j.epsl.2012.10.002>
- 880 Thigpen, J. R., Ashley, K. T., Law, R. D., 2017. Evaluating kinematic displacement rate effects on transient
881 thermal processes in thrust belts using coupled thermomechanical finite-element models. In: Law, R. D., Thigpen,
882 J. R., Mersch, A. J., Stowell H. H. (Ed.), *Linkage and feedbacks in orogenic systems* 213, 1–23. *Geological*
883 *Society of America Memoir*. [https://doi.org/10.1130/2017.1213\(01\)](https://doi.org/10.1130/2017.1213(01))
- 884 Thigpen, J. R., Ashley, K. T., Mako, C., Law, R. D., Spencer, B., 2021. Interplay between crustal-scale thrusting,
885 high metamorphic heating rates, and the development of inverted thermal-metamorphic gradients: Numerical
886 models and examples from the Caledonides of northern Scotland. *Tectonics*, 40, e2021TC006716.
887 <https://doi.org/10.1029/2021TC006716>
- 888 Thigpen, J.R., Law, R.D., Lloyd, G.E., Brown, S.J., Cook, B., 2010. Deformation temperatures, vorticity of flow
889 and strain symmetry in the Loch Eriboll mylonites, NW Scotland: implications for the kinematic and structural
890 evolution of the northernmost Moine Thrust zone. *Geological Society of London, Special Publications* 335, 623–
891 662. <https://doi.org/10.1144/sp335.26>

- 892 Thigpen, J.R., Law, R.D., Loehn, C., Strachan, R.A., Tracy, R., Lloyd, G., Roth, B., Brown, S., 2013. Thermal
893 structure and tectonic evolution of the Scandian orogenic wedge, Scottish Caledonides: Integrating
894 geothermometry, deformation temperatures, and kinematic-thermal modeling. *Journal of Metamorphic Geology*
895 31, 813–842. <https://doi.org/10.1111/jmg.12046>
- 896 Tikoff, B., Fossen, H., 1995. The limitations of three-dimensional kinematic vorticity analysis. *Journal of*
897 *Structural Geology* 17, 1771–1784.
- 898 Vai, G.B., Coccozza, T., 1974. Il “postgotlandiano” sardo, unità sinorogenica ercinica. *Bollettino della Società*
899 *Geologica Italiana* 93, 61–72.
- 900 Vidal, O., Lanari, P., Munoz, M., Bourdelle, F., De Andrade, V., 2016. Deciphering temperature, pressure and
901 oxygen-activity conditions of chlorite formation, *Clay Minerals*, 51, 615–633
902 <https://doi.org/10.1180/claymin.2016.051.4.06>
- 903 Vitale, S., Mazzoli, S., 2008. Heterogeneous shear zone evolution: the role of shear strain hardening/softening.
904 *Journal of Structural Geology* 30, 1383–1395.
- 905 Vitale Brovarone, A., Beyssac, O., Malavieille, J., Molli, G., Beltrando, M., Compagnoni, R., 2013. Stacking and
906 metamorphism of continuous segments of subducted lithosphere in a high-pressure wedge: The example of Alpine
907 Corsica (France). *Earth-Science Reviews* 116, 35–56. <https://doi.org/10.1016/j.earscirev.2012.10.003>
- 908 Vitale Brovarone, A., Tumiati, S., Piccoli, F., Ague, J. J., Connolly, J. A. D., Beyssac, O., 2020. Fluid-mediated
909 selective dissolution of subducting carbonaceous material: Implications for carbon recycling and fluid fluxes at
910 forearc depths, *Chemical Geology* 549, 119682, <https://doi.org/10.1016/j.chemgeo.2020.119682>
- 911 Vollmer, FW., 2015. EllipseFit 3.2. <https://www.frederickvollmer.com/ellipsefit/>
- 912 Wallis, S.R., Platt, J.P., Knott, S.D., 1993. Recognition of synconvergence extension in accretionary wedges with
913 examples from the Caiabrian Arc and the Eastern Alps. *American Journal of Science* 293, 463–495.
914 <https://doi.org/10.2475/ajs.293.5.463>
- 915 Wang, L., Cao, D.Y., Peng, Y.W., Ding, Z.Y., Li, Y., 2019b. Strain-induced graphitization mechanism of coal-
916 based graphite from Lutang, Hunan Province, China. *Minerals* 9(10), 617. <https://doi.org/10.3390/min9100617>
- 917 Waters, D.J., Law, R.D., Searle, M.P., Jessup, M., 2018, Structural and thermal evolution of the South Tibetan
918 Detachment shear zone in the Mt. Everest region, from the 1933 sample collection of L.R. Wager, in Ferrero, S.,
919 Lanari, P., Goncalves, P., and Grosch, E., eds., *Metamorphic Geology: Microscale to Mountains Belts: Geological*
920 *Society of London, Special Publication* 478, 38 p., <https://doi.org/10.1144/SP478.17>

- 921 Whitney, D., Evans, B., 2010. Abbreviations for names of rock-forming minerals. *American Mineralogy* 95, 185–
922 187. <https://doi.org/10.2138/am.2010.3371>
- 923 Willis, K., Houseman, G. A., Evans, L., Wright, T., Hooper, A., 2019. Strain localization by shear heating and the
924 development of lithospheric shear zones, *Tectonophysics* 764, 62–76. <https://doi.org/10.1016/j.tecto.2019.05.010>
- 925 Yonkee, A., 2005. Strain patterns within part of the Willard thrust sheet, Idaho-Wyoming-Utah thrust belt. *Journal*
926 *of Structural Geology* 27, 1315-1343. <https://doi.org/10.1016/j.jsg.2004.06.014>
- 927 Xypolias, P., 2010. Vorticity analysis in shear zones: A review of methods and applications. *Journal of Structural*
928 *Geology* 32, 2072–2092. <https://doi.org/10.1016/j.jsg.2010.08.009>
- 929



930

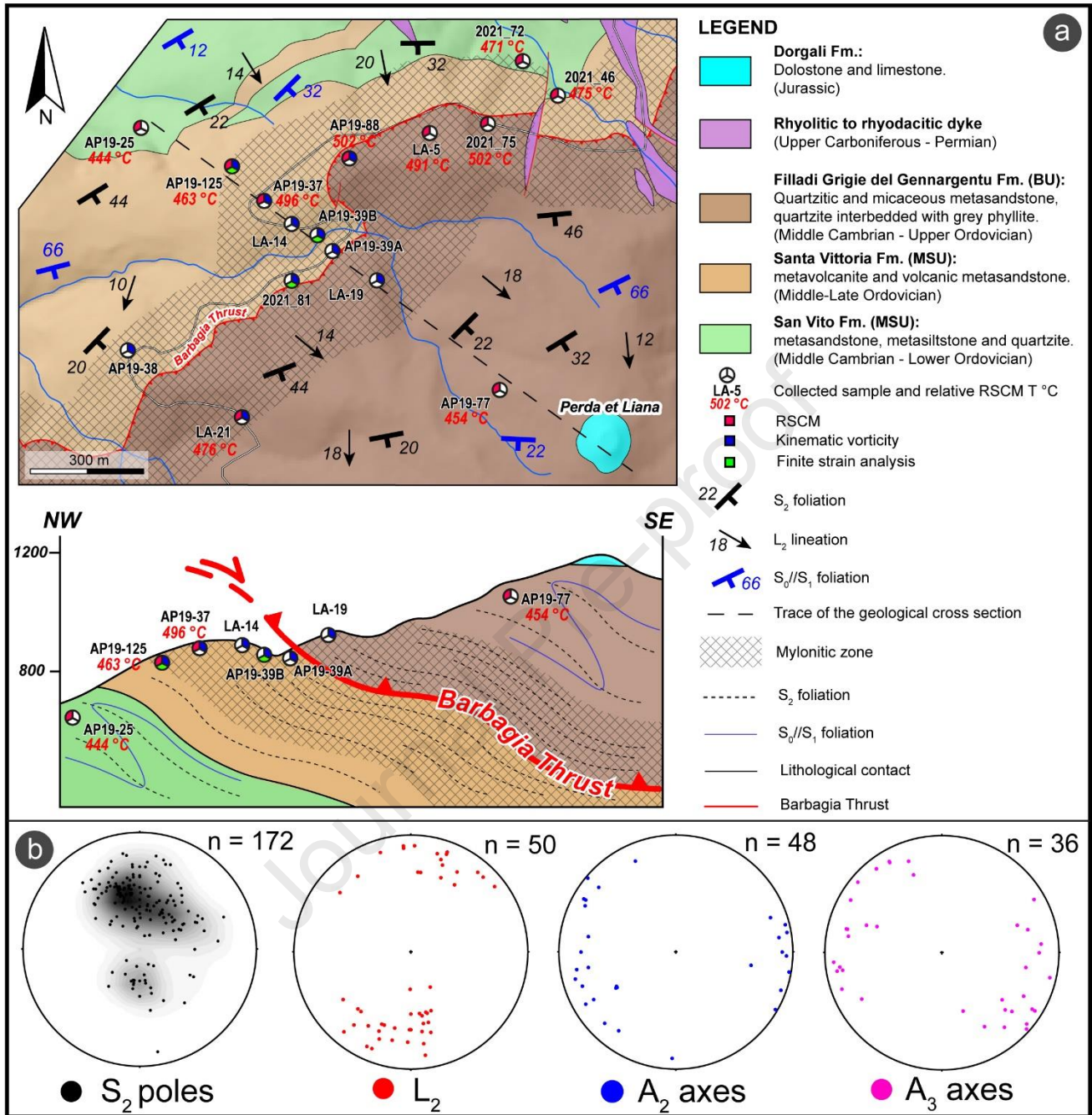
931 Fig. 1: a) Geographic position and tectonic sketch map of the Sardinia Island (modified from Carmignani et al., 1994).

932 Location of Fig. 1b is indicated; b) Schematic geological map of the Internal and External Nappe Zone in the central Sardinia.

933 The location of Area I and Area II has been highlighted. The trace of the geological cross-section A-A''' is indicated (modified

934 from Carmignani et al., 1994, 2015); c) Geological A-A''' cross-section along the Internal and External Nappe Zone. The

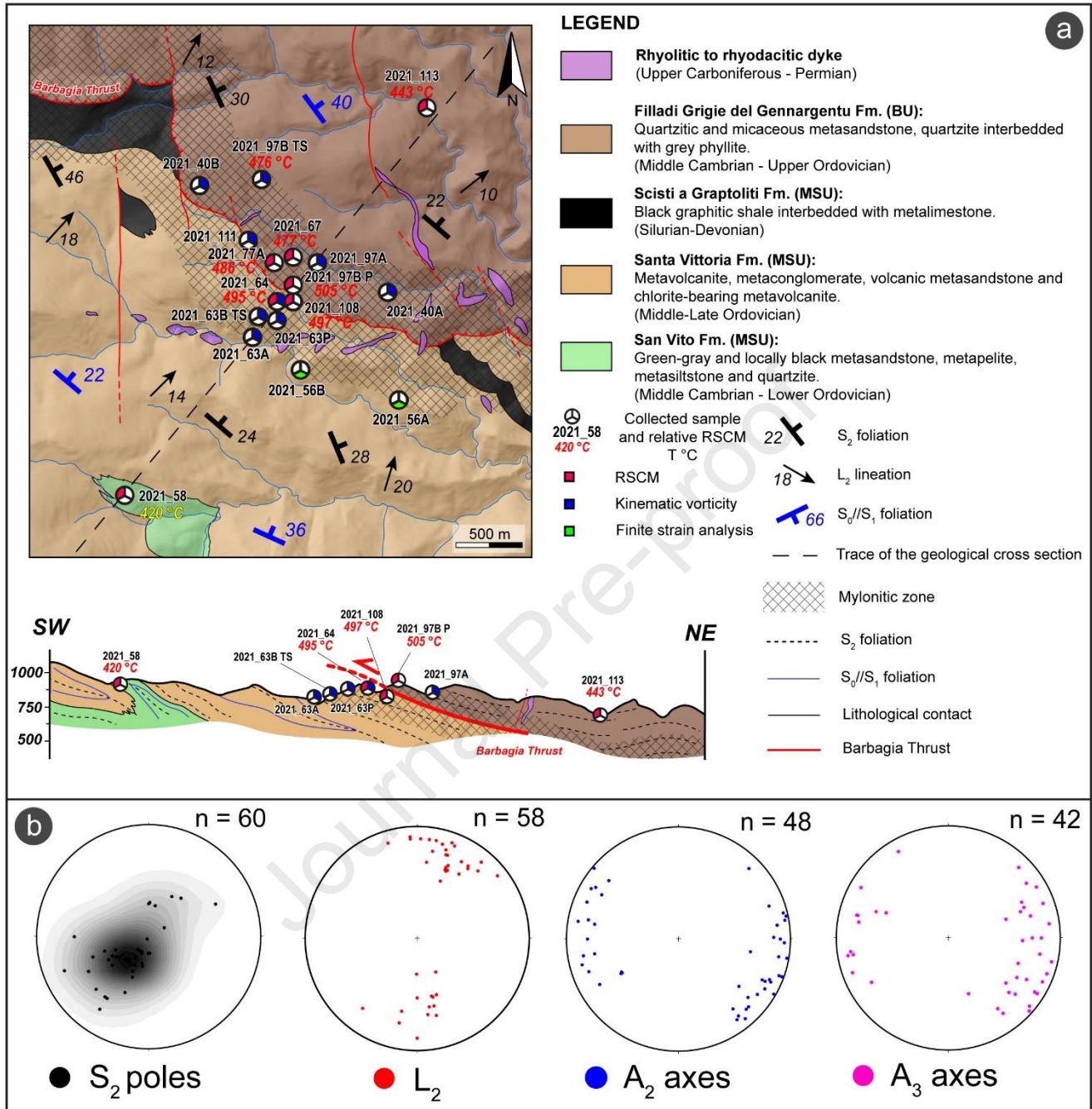
935 deep structure of the Barbagia Synform is uncertain. The horizontal and vertical exaggeration is for both 1.5:1.



936

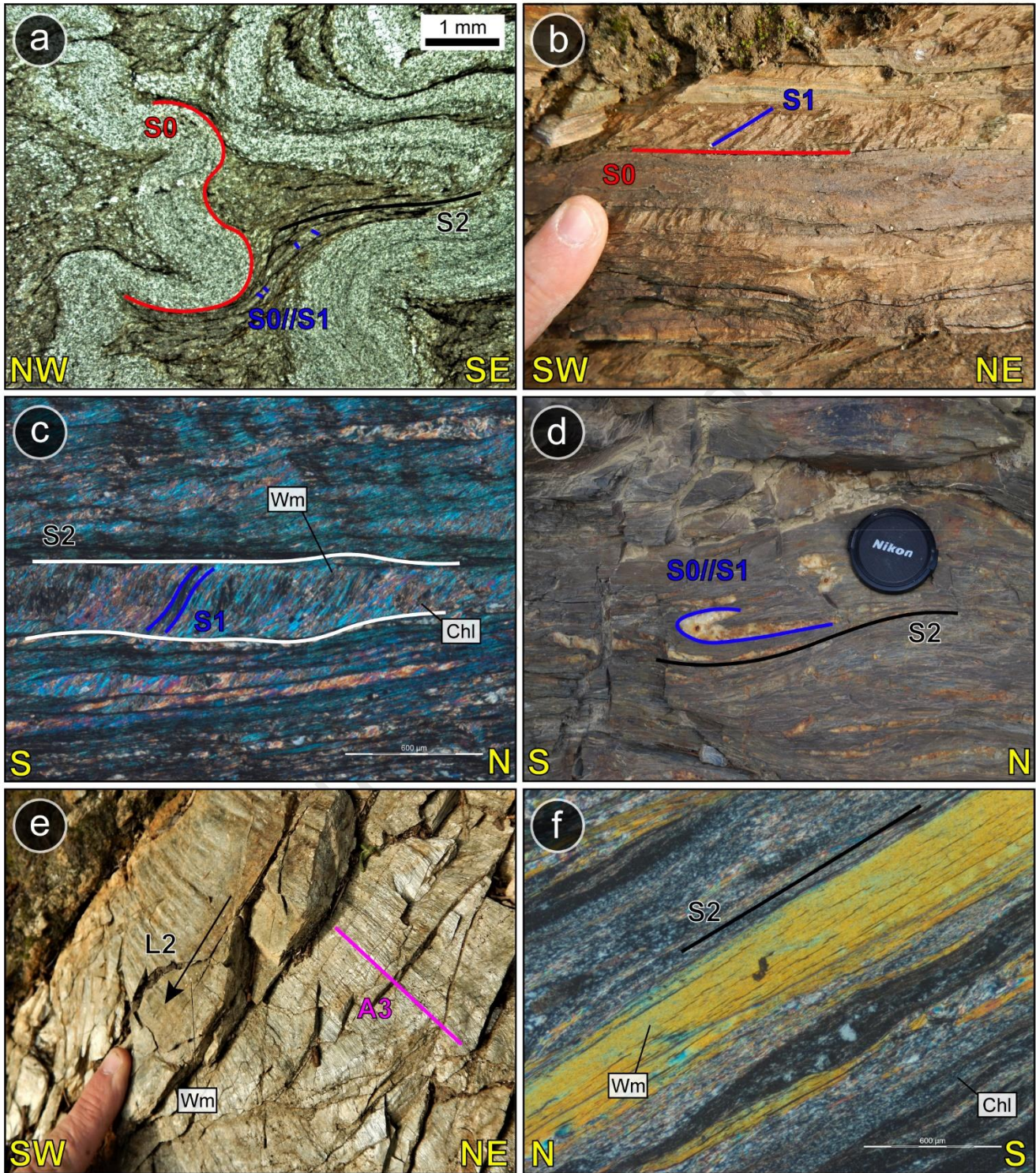
937 Fig. 2: a) Geological map of Area I, derived from our original fieldwork and mapping. The trace of NW-SE oriented geological
 938 cross-section, shown below (the vertical exaggeration is 2:1), is indicated. On the cross-section the selected samples locations
 939 and the corresponding type of analysis are indicated; b) Stereoplots (equal angle, lower hemisphere projections) of the main
 940 structural elements.

941



942

943 Fig. 3: a) Geological map of Area II (modified and integrated from Carosi, 2004). The trace of the NW-SE oriented geological
 944 cross-section, shown below (no vertical exaggeration) is indicated. On the cross-section the selected samples locations and
 945 the corresponding type of analysis are indicated; b) Stereoplots (equal angle, lower hemisphere projections) of the main
 946 structural elements.



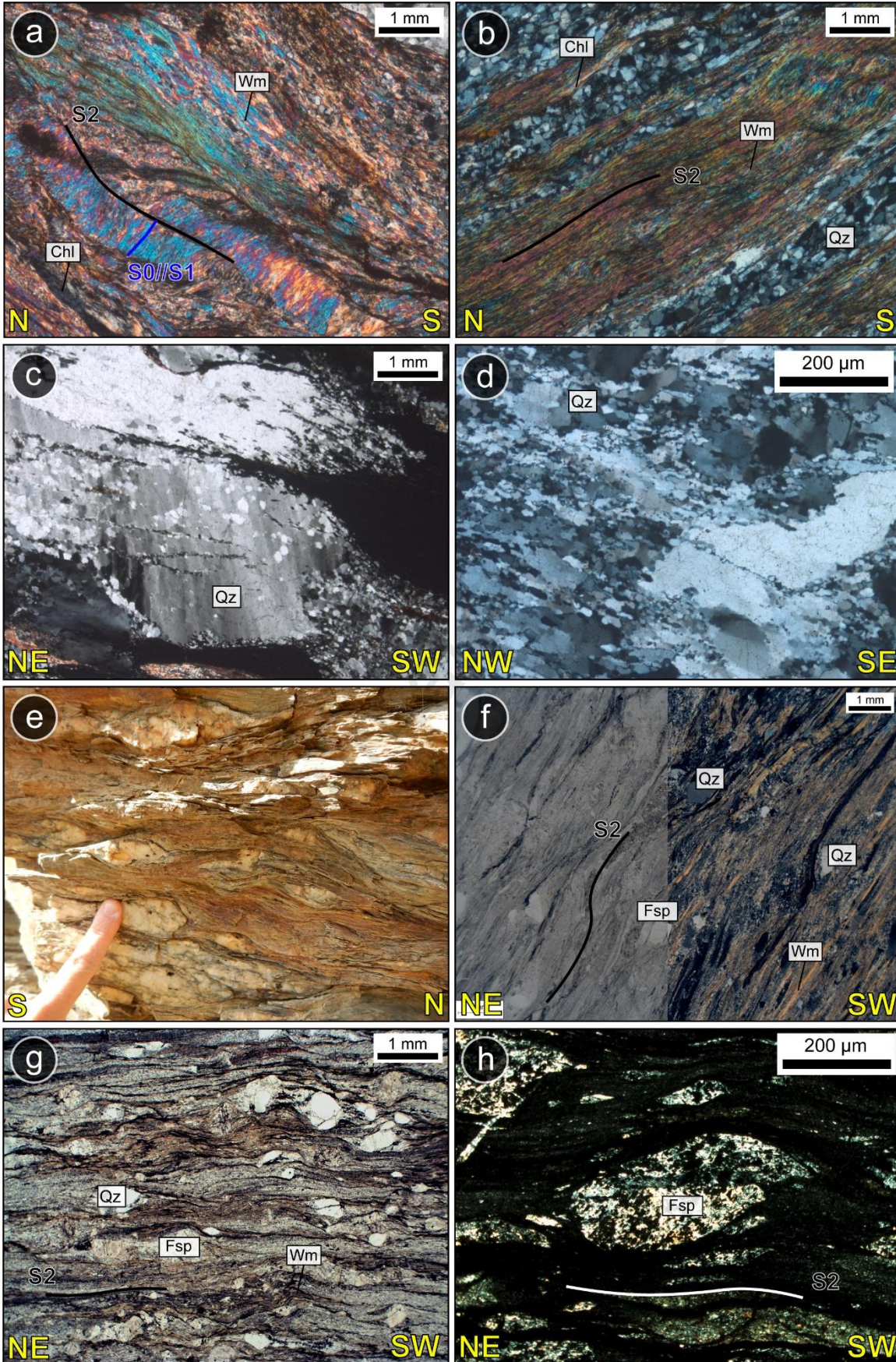
947

948 Fig. 4: a) S_2 spaced foliation with S_0/S_1 preserved in microlithons. A relict of bedding (S_0), defined by the primary
 949 compositional alternation between quartz-rich and phyllosilicate-rich levels, is recognizable (PPL: parallel-polarised light)
 950 (San Vito Fm.; FW); b) Selective S_1 foliation involving the S_0 compositional alternation in metasedimentary rock (Filladi

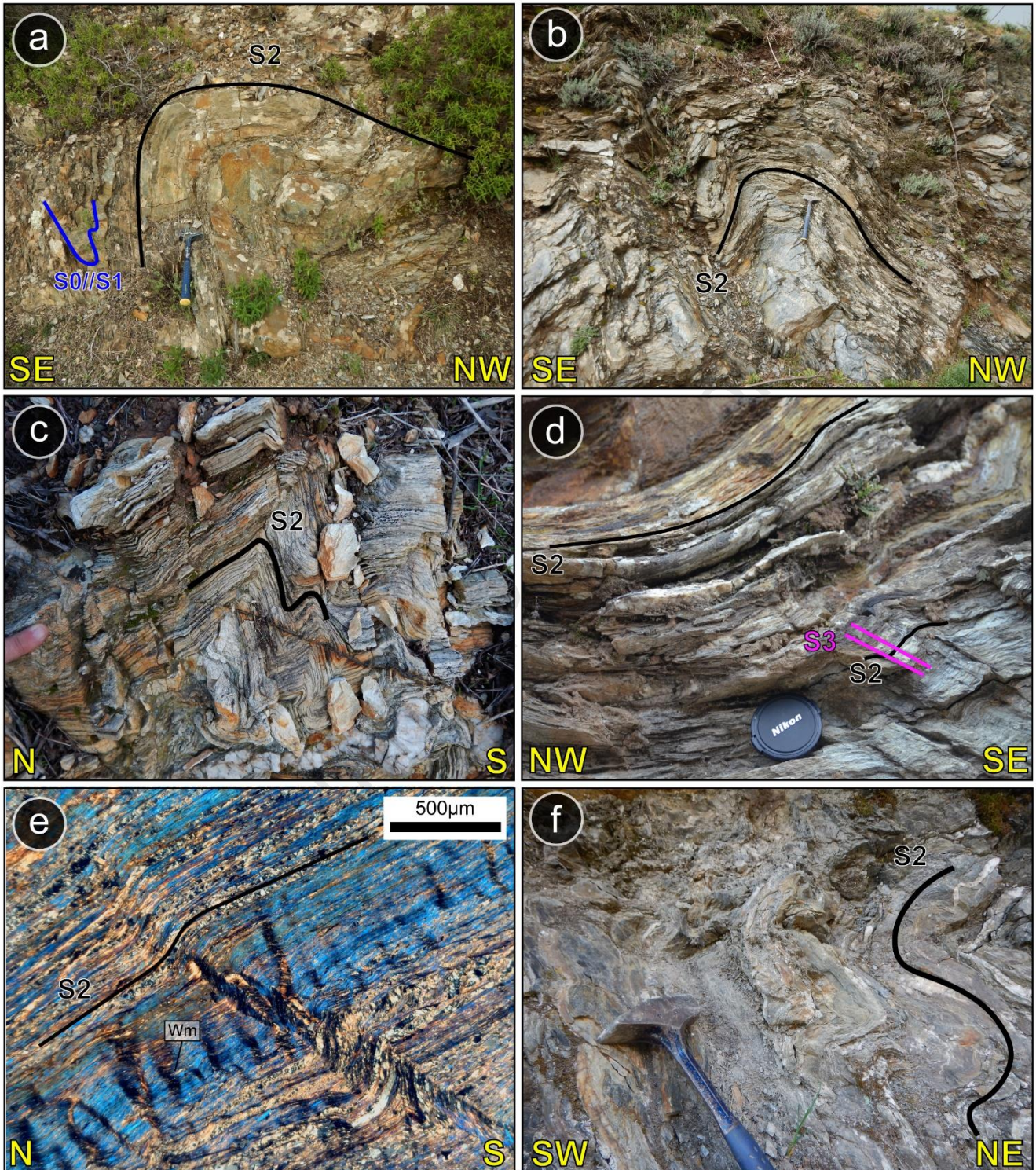
951 Grigie del Gennargentu Fm.; HW); c) S_2 spaced foliation at the microscale. S_1 preserved in microlithons is defined by
952 $Wm+Chl$ (XPL: crossed-polarised light) (San Vito Fm.; FW); d) Outcrop evidence of F_2 rootless fold. S_0/S_1 foliation is
953 preserved in the hinge of F_2 folds. The S_2 cleavage is parallel to the F_2 axial plane (Filladi Grigie del Gennargentu Fm.; HW);
954 e) L_2 object lineation, defined by Wm crystals and the intersection lineation, parallel to the A_3 fold axes, are displayed (San
955 Vito Fm.; FW); f) S_2 fine-grained continuous foliation defined by $Wm+Chl$ alternating with quartz-rich levels in
956 metasedimentary rocks (XPL) (San Vito Fm.; FW).

957

Journal Pre-proof



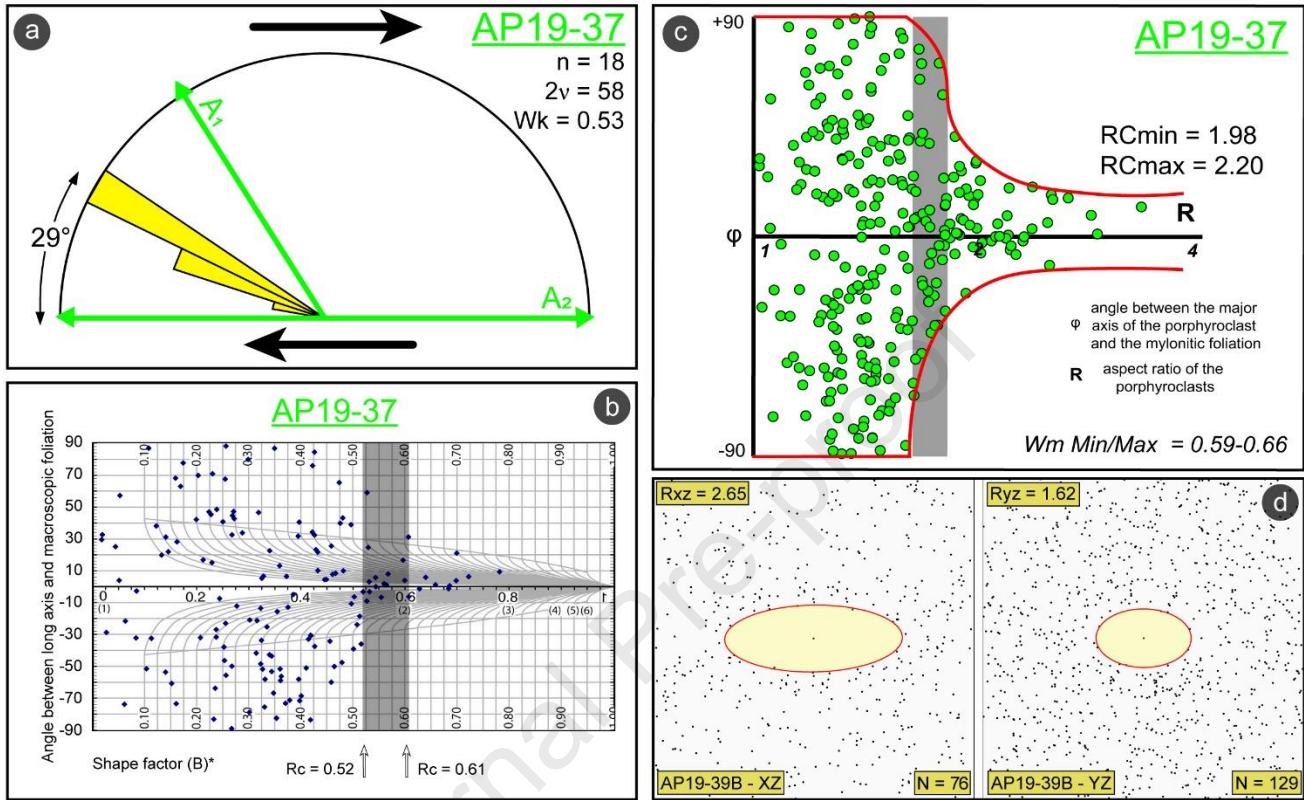
959 Fig. 5: Meso- and micro-scale features across the BT mylonitic zone. a) S_2 spaced foliation in metasedimentary rocks (San
960 Vito Fm.; FW). Both S_1 and S_2 cleavages are defined by Wm+Chl (XPL); b) Continuous cleavage in metasedimentary rocks
961 (Filladi Grigie del Gennargentu Fm.; HW). S_2 cleavage is defined by both quartz and phyllosilicate-rich horizons (XPL)
962 (Filladi Grigie del Gennargentu Fm.; HW); c) quartz with small new-grains and undulose extinction indicative of BLG II
963 mechanism (XPL) (Filladi Grigie del Gennargentu Fm.; HW); d) quartz with BLG II and minor local SGR mechanisms in a
964 mylonite, subgrains, and new grains can be recognized (XPL) (Filladi Grigie del Gennargentu Fm.; HW); e) HW mylonites
965 at the mesoscale: mylonitic fabric indicating a sense of shear top-to-the S (Filladi Grigie del Gennargentu Fm.); f) FW
966 mylonite at the microscale: C' -S fabric is indicative of a top-to-the SW sense of shear (PPL and XPL) (San Vito Fm.); g) FW
967 metavolcanoclastic mylonitic rocks. C' -S fabric and rotated porphyroclasts pointing to a top-to-the SW sense of shear (PPL)
968 (Santa Vittoria Fm.); h) Fine-grained continuous cleavage and sigma-type porphyroclast in the FW ultramylonite indicating
969 a top-to-the SW sense of shear (XPL) (Santa Vittoria Fm.).



970

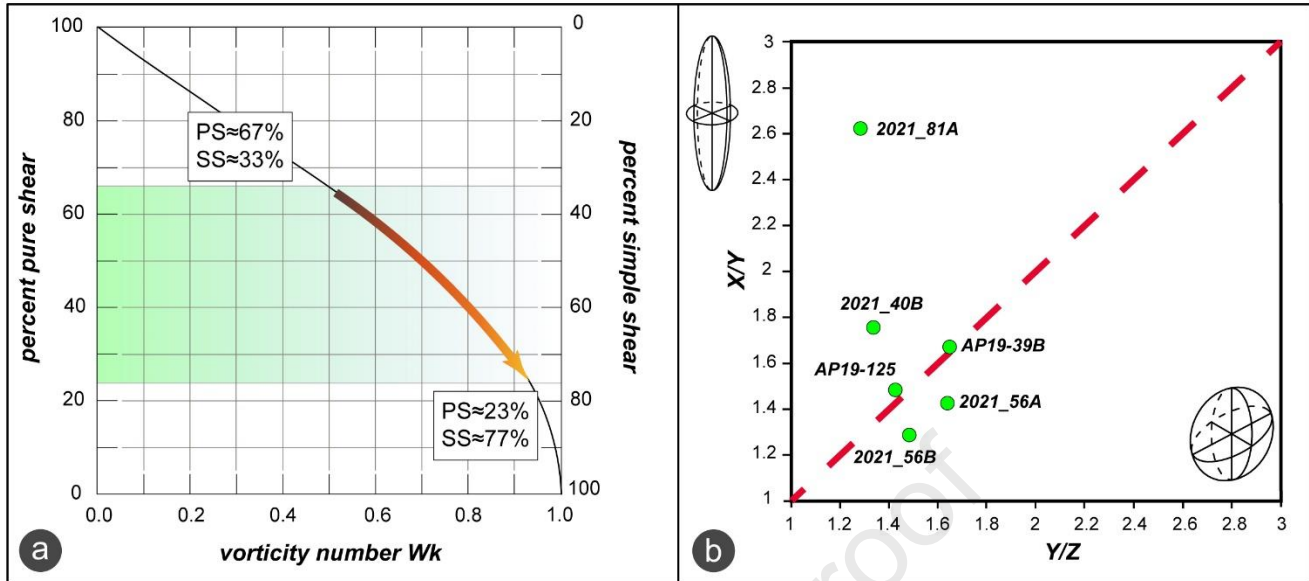
971 Fig. 6: Outcrop aspect of the F₃ (a) asymmetric, (b) upright and (c) kink folds, showing mainly S-SE vergence; d) S₃ spaced972 foliation at mesoscale developed only in less competent layers in the hinge of F₃ fold; e) Continuous S₂ foliation, defined by

973 Wm+Chl, deformed by F_3 micro-kink folds (XPL); f) Outcrop evidence of late open folds (F_4) with sub-horizontal axes and
 974 axial planes, deforming S_2 foliation.



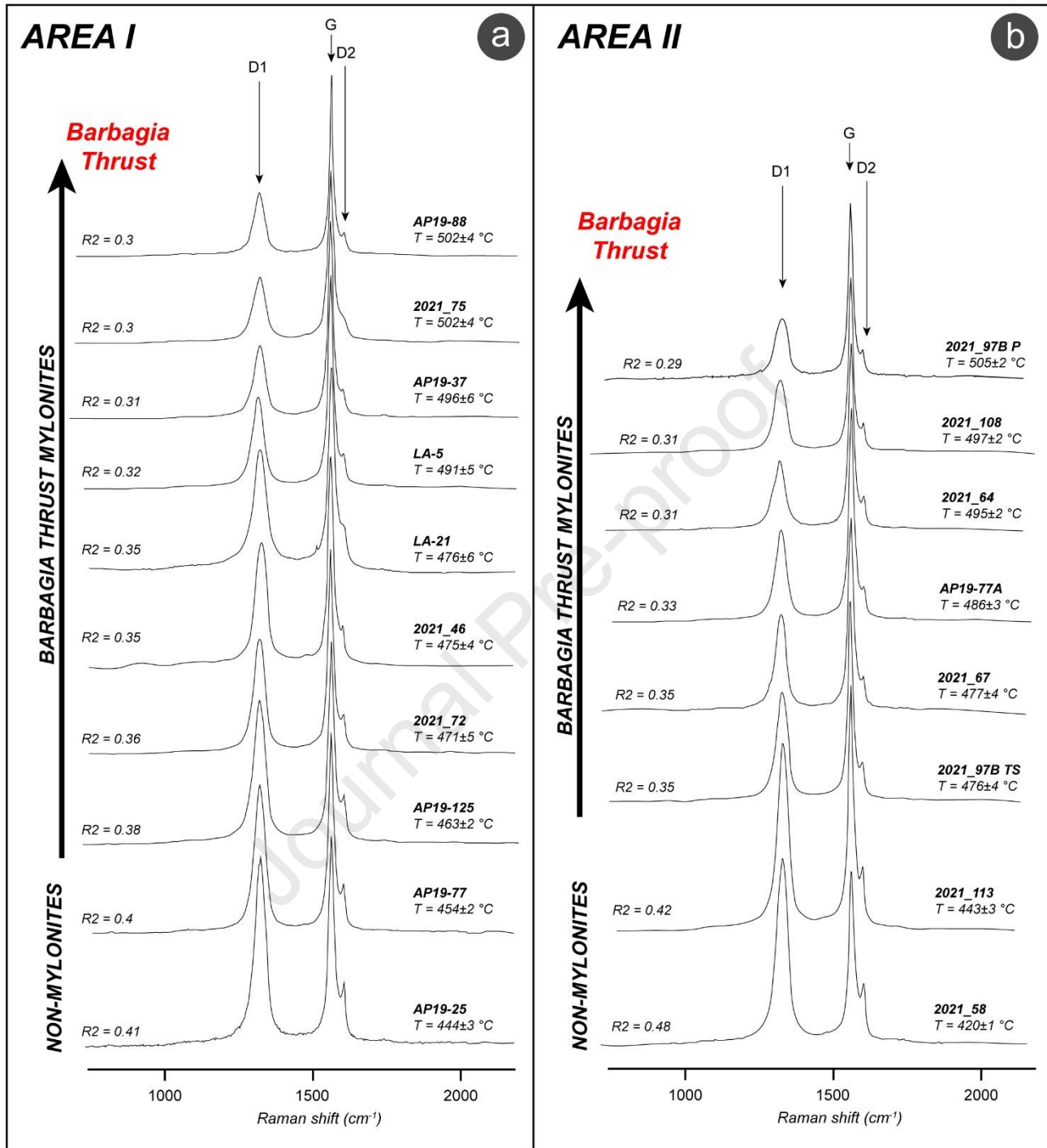
975

976 Fig. 7: Example of vorticity analysis and finite strain results. a) Polar histogram used to derive the angle v , and the
 977 corresponding kinematic vorticity number, Wk . A_1 = flow apophysis 1; A_2 = flow apophysis 2; n = total number of data; b)
 978 and c) Example of the plots for the porphyroclasts-based methods (b=RGN; c= stable porphyroclasts method). Rc_{min} and
 979 Rc_{max} = minimum and maximum critical axial ratio; Wm = mean kinematic vorticity number; d) Fry diagram for the XZ and
 980 YZ sections of the finite strain ellipsoid. N = number of centers considered in the analysis. The R_{XZ} and R_{YZ} axial ratios are
 981 shown.



982

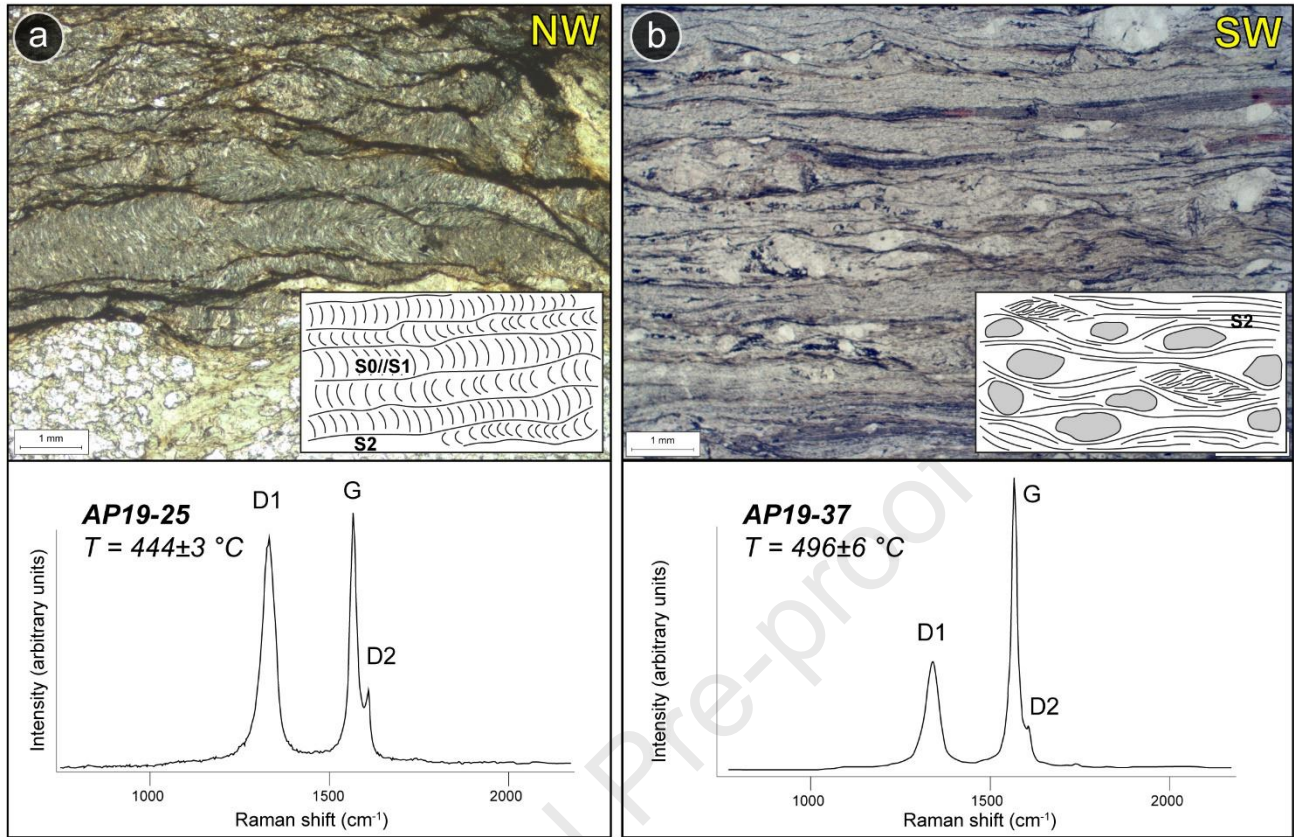
983 Fig. 8: a) Diagram showing the relative percentage of simple shear obtained from the selected samples of both areas. The
 984 simple shear component increases (highlighted by the arrow) according to deformation gradient; b) Flinn diagram showing
 985 the analyzed samples (green dots) finite strain results (for sample location see figure 2a, 3a).



986

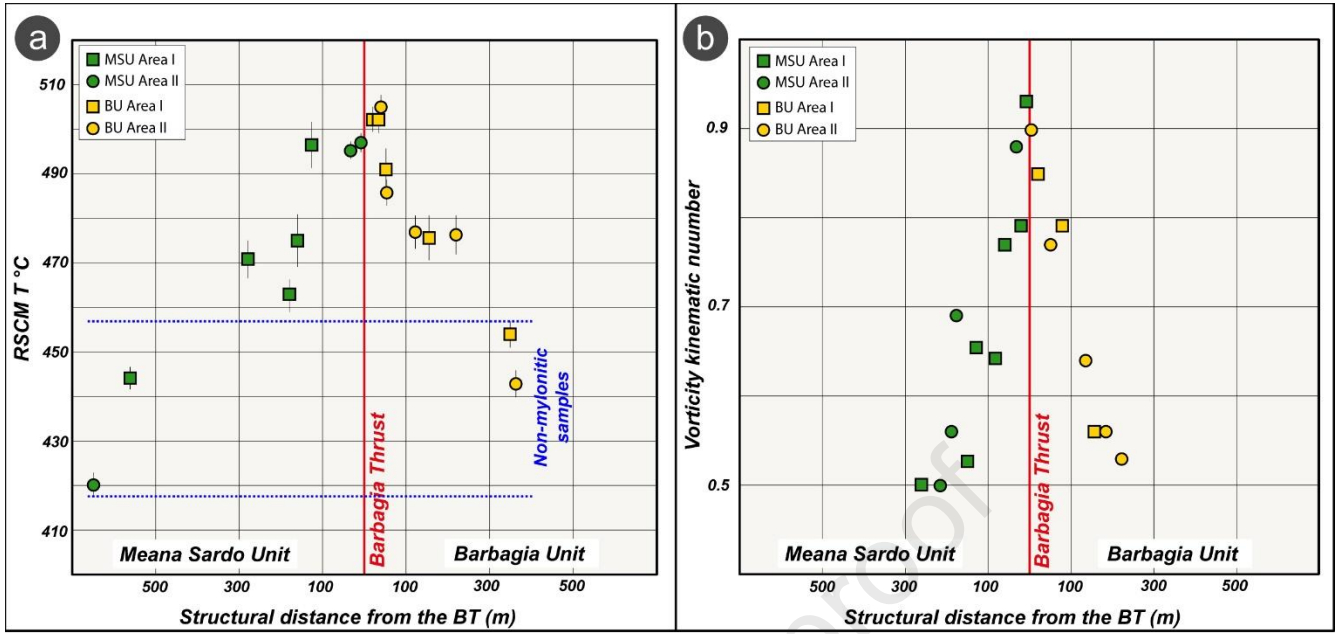
987 Fig. 9: Raman spectra of carbonaceous material obtained in non- and mylonitic rocks of both investigated areas for Area I (a)
 988 and Area II (b). For each spectrum, the R2 ratio and the corresponding RSCM T (°C) with the relative simplified error have
 989 been indicated. Samples are ordinated according to structural distance from the Barbagia Thrust.

990



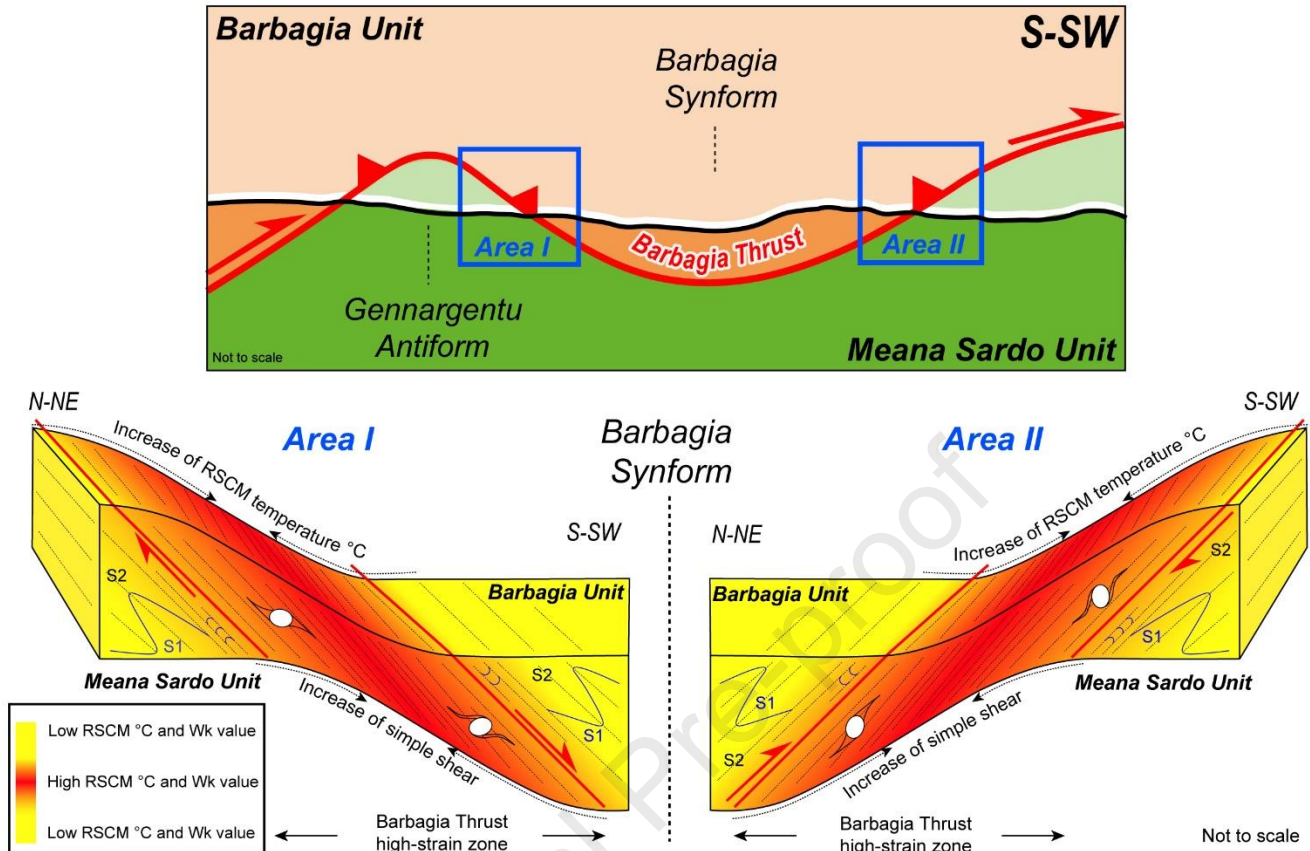
991

992 Fig. 10: Example from the Area I of the variation of RSCM temperature in different deformed rocks. Thin sections (PPL) and
 993 representative Raman spectra for carbonaceous material from FW samples AP19-25 (a) and AP19-37 (b), respectively outside
 994 and inside the mylonitic zone (see Fig. 2a for the position of the samples). Note that the RSCM T ($^\circ\text{C}$) is higher in the mylonite.



995

996 Fig. 11: a) Distribution of RSCM T ($^{\circ}\text{C}$) compared with the sample structural distance with respect to the BT. b) Distribution
 997 of estimated vorticity kinematic number against the structural distance from the BT. Both graphs show increasing RSCM T
 998 ($^{\circ}\text{C}$) and Wk values (i.e., increase in simple shear) toward the shear zone.



999

1000 Fig. 12: On the top, the current stage of the architecture of the belt is shown by a simplified cross-section across the Internal
 1001 and External Nappe Zone. We highlighted the approximated position of the investigated areas and the simplified present-day
 1002 topography. The sense of shear is the same in both areas, pointing to a top-to-to-the S/SW. On the bottom, not to scale
 1003 representations of the Barbagia Thrust along with the northern and southern limb of the Barbagia Synform have been
 1004 displayed. The given "finite" shape is not referred to the shear displacement but due to the late fold (F_3) linked to D_3
 1005 deformation (Barbagia Synform). The progressive strain partitioning and gradient, from fold structures to a mylonitic foliation
 1006 (approaching the BT high-strain zone), have been highlighted, mirrored by the increase of both simple shear and the RSCM
 1007 T ($^{\circ}\text{C}$).

1008

1009

1010

Area I																								
RSCM analysis												Kinematic vorticity and finite strain analysis												
SAMPLE NAME	UNIT	DISTANCE FROM THE BT (m)	n.	R2	Aoya et al., 2010			Beysac et al.,			N	v ANGLE (°)	Wk	RGN			Porphyroclasts method			Finite strain analysis				
					SD	SE (°C)	RSCM °C	SD	SE (°C)	RSCM °C				N	Wm	Rc min	Rc max	Wk min	Wk max	Wk mid	R _{xz}	R _{yz}	R _{xy}	K
AP19-77	BU	350	10	0.40	5.7	1.9	454	5.6	1.9	464	-	-	-	-	-	-	-	-	-	-	-			
LA-21	BU	156	12	0.35	18.1	5.5	476	16.8	5.1	486	18	28	0.56	-	-	-	-	-	-	-	-			
LA-19	BU	80	-	-	-	-	-	-	-	-	9	19	0.79	-	-	-	-	-	-	-	-			
LA-5	BU	52	12	0.32	17.2	5.2	491	15.6	4.7	498	-	-	-	-	-	-	-	-	-	-	-			
2021_75	BU	22	11	0.30	14.0	4.4	502	12.4	3.9	508	-	-	-	-	-	-	-	-	-	-	-			
AP19-88	BU	18	11	0.30	13.4	4.2	502	11.9	3.8	508	22	16	0.85	-	-	-	-	-	-	-	-			
AP19-39A	MSU	10	-	-	-	-	-	-	-	-	11	11	0.93	-	-	-	-	-	-	-	-			
2021_81A	MSU	16	-	-	-	-	-	-	-	-	14	19	0.79	-	-	-	-	-	-	3.30	1.26	2.62	6.23	
AP19-39B	MSU	60	-	-	-	-	-	-	-	-	22	20	0.77	-	-	-	-	-	-	2.65	1.62	1.64	1.03	
AP19-38	MSU	84	-	-	-	-	-	-	-	-	18	25	0.64	-	-	-	-	-	-	-	-	-	-	
LA-14	MSU	122	-	-	-	-	-	-	-	-	-	-	-	164	0.56 - 0.65	2.11	2.33	0.63	0.69	0.66	-	-	-	-
AP19-37	MSU	126	10	0.31	17.4	5.8	496	15.6	5.2	503	18	29	0.53	280	0.52 - 0.61	1.98	2.20	0.59	0.66	0.63	-	-	-	-
2021_46	MSU	160	15	0.35	13.5	3.6	475	12.5	3.3	483	-	-	-	-	-	-	-	-	-	-	-	-	-	
2021_72	MSU	178	16	0.36	17.7	4.6	471	16.4	4.2	480	-	-	-	-	-	-	-	-	-	-	-	-	-	
AP19-125	MSU	280	10	0.38	5.2	1.7	463	4.9	1.6	472	22	30	0.50	-	-	-	-	-	-	2.18	1.42	1.54	1.27	
AP19-25	MSU	560	10	0.41	8.2	2.7	444	8.1	2.7	455	-	-	-	-	-	-	-	-	-	-	-	-	-	

Area II																								
RSCM analysis												Kinematic vorticity and finite strain analysis												
SAMPLE NAME	UNIT	DISTANCE FROM THE BT (m)	n.	R2	Aoya et al., 2010			Beysac et al.,			N	v ANGLE (°)	Wk	RGN			Porphyroclasts method			Finite strain analysis				
					SD	SE (°C)	RSCM °C	SD	SE (°C)	RSCM °C				N	Wm	Rc min	Rc max	Wk min	Wk max	Wk mid	R _{xz}	R _{yz}	R _{xy}	K
2021_113	BU	360	12	0.42	8.3	2.5	443	8.2	2.5	454	-	-	-	-	-	-	-	-	-	-	-	-	-	-
2021_97B TS	BU	220	16	0.35	16.3	4.2	476	14.8	3.8	485	15	29	0.53	-	-	-	-	-	-	-	-	-	-	-
2021_97A	BU	180	-	-	-	-	-	-	-	-	17	28	0.56	-	-	-	-	-	-	-	-	-	-	-
2021_40A	BU	135	-	-	-	-	-	-	-	-	18	25	0.64	-	-	-	-	-	-	-	-	-	-	-
2021_67	BU	122	11	0.35	11.7	3.7	477	10.7	3.4	485	-	-	-	-	-	-	-	-	-	-	-	-	-	
AP19-77A	BU	55	10	0.33	8.6	2.9	486	7.8	2.6	494	-	-	-	-	-	-	-	-	-	-	-	-	-	
2021_40B	BU	52	-	-	-	-	-	-	-	-	12	20	0.77	-	-	-	-	-	-	2.42	1.36	1.78	2.17	
2021_97B P	BU	40	12	0.29	6.5	2	505	5.7	1.7	511	-	-	-	-	-	-	-	-	-	-	-	-	-	
2021_111	BU	12	-	-	-	-	-	-	-	-	7	13	0.90	-	-	-	-	-	-	-	-	-	-	-
2021_108	MSU	10	10	0.31	7.2	2.4	497	6.4	2.1	504	-	-	-	-	-	-	-	-	-	-	-	-	-	
2021_64	MSU	35	12	0.31	5.8	1.7	495	5.2	1.6	502	14	14	0.88	-	-	-	-	-	-	-	-	-	-	
2021_63B P	MSU	180	-	-	-	-	-	-	-	-	12	23	0.69	-	-	-	-	-	-	-	-	-	-	-
2021_63B TS	MSU	235	-	-	-	-	-	-	-	-	16	28	0.56	-	-	-	-	-	-	-	-	-	-	-
2021_63A	MSU	254	-	-	-	-	-	-	-	-	24	30	0.5	-	-	-	-	-	-	-	-	-	-	-
2021_56B	MSU	288	-	-	-	-	-	-	-	-	-	-	-	-	-	-	-	-	-	1.96	1.49	1.23	0.39	
2021_56A	MSU	300	-	-	-	-	-	-	-	-	-	-	-	-	-	-	-	-	-	2.25	1.63	1.38	0.61	
2021_58	MSU	650	18	0.48	5.5	1.3	420	5.7	1.4	429	-	-	-	-	-	-	-	-	-	-	-	-	-	

1011

1012 Table 1: Results of the RSCM estimations (both Aoya et al. (2010) and Beysac et al. (2002) calibrations results are indicated),
1013 kinematic vorticity, and the finite strain (see Figure 2 and Figure 3 for samples location). Samples, divided according to the
1014 corresponding tectonic unit, are listed according to the distance with respect to the BT. The number of spectra (n), mean R2
1015 ratio (Beysac et al., 2002) for n spectra with corresponding standard deviation (SD), and calculated temperature with standard
1016 error ($SE = SD/\sqrt{n}$) have been indicated.

1017

1018

Highlights

Temperature variations responsible for the dynamic weakening and localization of strain,

Paleothermal architecture fits with a tectonic scenario of shear heating coupled with a simple shear increase

The tectonic contact represents a full-fledged boundary that divides the internal sector of the Internal sector of the wedge to the external one

Journal Pre-proof

Declaration of competing interest

The authors declare that they have no competing financial interests or personal relationships that could have appeared to influence the work reported in this paper.

Journal Pre-proof